

Rowan University

Rowan Digital Works

Theses and Dissertations

6-23-2020

Polyimide/silicon dioxide nanocomposites as dielectrics for helium-cooled high-temperature superconducting cables

Harrison Michael Hones
Rowan University

Follow this and additional works at: <https://rdw.rowan.edu/etd>



Part of the [Electro-Mechanical Systems Commons](#)

Recommended Citation

Hones, Harrison Michael, "Polyimide/silicon dioxide nanocomposites as dielectrics for helium-cooled high-temperature superconducting cables" (2020). *Theses and Dissertations*. 2817.
<https://rdw.rowan.edu/etd/2817>

This Thesis is brought to you for free and open access by Rowan Digital Works. It has been accepted for inclusion in Theses and Dissertations by an authorized administrator of Rowan Digital Works. For more information, please contact graduateresearch@rowan.edu.

**POLYIMIDE/SILICON DIOXIDE NANOCOMPOSITES AS DIELECTRICS FOR
HELIUM-COOLED HIGH-TEMPERATURE SUPERCONDUCTING CABLES**

by

Harrison Michael Hones

A Thesis

Submitted to the
Department of Mechanical Engineering
Henry M. Rowan College of Engineering
In partial fulfillment of the requirement
For the degree of
Master of Science in Mechanical Engineering
at
Rowan University
May 29, 2020

Thesis Advisors: Wei Xue, Ph.D., and Robert R. Krchnavek, Ph.D.

© 2020 Harrison Michael Hones

Dedications

I would like to dedicate this manuscript to my family, who have never failed to support and inspire me. I want to thank my parents – Mary and Harry Hones – for seeing potential in me even when I could not. I also want to thank my siblings – Brenna, Logan, and Ethan Hones – for showing me how to be the best version of myself. The five of you have made this part of my life’s journey possible, I could not have done it without you.

Acknowledgments

I would like to express my gratitude to my professor, Dr. Wei Xue. These last two years as your graduate student have changed my life in countless ways. Your help and guidance have pushed me to be a better student, researcher, and person. Further, I would like to thank Dr. Robert Krchnavek for his encouragement and guidance and on this research.

I want to extend my thanks to my friends and lab mates, Muhammet E. Cavusoglu and Rhandy Paladines for the laughs and the memories made in our lab. Special thanks to Michael McCaffrey for showing me how to lead a research group, and for keeping my optimism in check. Finally, special thanks to Jordan Cook for always pushing me to work harder, and for answering my countless questions of “Does this look/sound okay?”

Additionally, I want to thank the undergraduate students who were enrolled in the “Polymer Nanocomposites for Navy Applications” Junior/Senior Engineering Clinics at Rowan University for their hard work. Every one of you had a significant impact, either on this research or on me personally.

Finally, the work reported herein was supported by the Department of Defense under the Naval Surface Warfare Center (NSWC), and the Naval Engineering Education Consortium (NEEC) with the grant number NSWC IHEODTD N00174-17-1-0008 and in part by the National Science Foundation with the grant number CBET #1625816. A special thanks to the Applied Superconductivity team at the Naval Surface Warfare Center Philadelphia Division for their guidance and discussion on cryogenic testing of dielectrics and cryogenic systems.

Abstract

Harrison Michael Hones
POLYIMIDE/SILICON DIOXIDE NANOCOMPOSITES AS DIELECTRICS FOR
HELIUM-COOLED HIGH-TEMPERATURE SUPERCONDUCTING CABLES
2019-2020

Wei Xue, Ph.D., and Robert R. Krchnavek, Ph.D.
Master of Science in Mechanical Engineering

In this thesis, polyimide (PI) and silicon dioxide (SiO_2) were combined in the form of a nanocomposite for use as a dielectric on helium-cooled high-temperature superconducting (HTS) cables. Further, a cryogenic chamber was designed with the intent of cooling samples to 40 K for dielectric and thermal contraction testing. Composites were created through an in situ process which resulted in nanoparticle formation within the host matrix. Samples were tested for dielectric strength at room temperature (300 K) as well as cryogenic temperature (92 K) using liquid nitrogen as the coolant. Composite samples tested at 300 K averaged a dielectric strength of about 175 kV/mm, while those tested cryogenically exhibited an average strength of around 275 kV/mm. Samples were imaged via scanning electron microscopy (SEM) both before and after dielectric testing. Imaging samples broken down at 92 K revealed evidence of electrical treeing, a breakdown mechanism discussed in this thesis. Finally, the helium chamber has been designed to accommodate multiple testing systems at cryogenic temperatures. Although this research is ongoing, the PI/ SiO_2 composite is already a promising candidate as a cryogenic HTS cable dielectric.

Table of Contents

Abstract	v
List of Figures	ix
List of Tables	xii
Chapter 1: Introduction	1
1.1. Naval Ships and HTS Cables	1
1.2. HTS Cable Applications	2
1.3. Dielectric Requirements.....	4
1.4. Nanocomposites	7
1.4.1 Host Matrix – Polyimide.....	8
1.4.2 Nanoparticle – Silicon Dioxide.....	9
1.5. Cryogenic Testing Chamber	10
1.6. Motivation and Objectives	12
1.7. General Layout of Thesis.....	12
Chapter 2: Nanocomposite Fabrication	14
2.1. Nanoparticle Distribution.....	14
2.1.1. Ex Situ Method.....	15
2.1.2. In Situ Method.....	15
2.2. Thin Film Preparation	18
2.3. Discussion of Fabrication Methods	20

Table of Contents (Continued)

Chapter 3: Material Characterization.....	23
3.1. Dielectric Breakdown Testing	23
3.1.1. Dielectric Testing at Room Temperature	25
3.1.2. Dielectric Testing at Cryogenic Temperature	27
3.2. Scanning Electron Microscopy	30
3.2.1. Energy-Dispersive X-Ray Spectroscopy	31
Chapter 4: Characterization Results.....	32
4.1. Dielectric Strength	32
4.2. SEM Imaging	34
4.2.1. EDS Imaging	36
4.3. Breakdown Point Imaging	37
4.4. Evidence of Treeing in Broken Down Samples.....	41
Chapter 5: Cryogenic Testing Chamber	43
5.1. Design Considerations	43
5.2. Inner Chamber Design	47
5.3. Outer Chamber Design	50
5.4. Chamber Simulations.....	52
Chapter 6: Conclusions and Future Works	55

Table of Contents (Continued)

6.1. Summary	55
6.2. Future Works	57
References	61

List of Figures

Figure	Page
Figure 1. Three phase superconducting cable, with each phase separated by a dielectric, contained within a cryostat [5].	2
Figure 2. Layout of HTS cables along the hull of a Navy ship. HTS cables are indicated by grey lines running vertically and horizontally [12].	3
Figure 3. Schematic view of the HTS cable system installed in the Albany Project. The HTS cable runs underground to connect two termination boxes [17].	4
Figure 4. Schematic of helium atoms permeating layers of lapped dielectric tape.	5
Figure 5. Contraction rates of common cryogenic materials, notably HTS cable cores and polymers [24].	6
Figure 6. An example of how a dielectric layer with a large CTE could fail when coated on an HTS cable with a lower CTE.	7
Figure 7. Schematic of a nanocomposite. The host matrix is depicted in yellow, while the nanoparticles are shown in grey.	8
Figure 8. Chemical structure for PAA. The elements present are hydrogen, nitrogen, and oxygen [28].	9
Figure 9. Silica particles purchased from Sigma-Aldrich, 20 nm (left) and 80 nm (right) in diameter.	10
Figure 10. Gaseous helium-cooled cryogenic chamber designed to cool a section of HTS cable [41].	11
Figure 11. Chemical structures of PAA and PI transitioning through the imidization process [42].	14
Figure 12. Simplified chemical reactions of the Stöber process resulting in the formation of silica and water.	17
Figure 13. From initial precursors, the steps of nanoparticle formation over time during the sol gel process [47].	17
Figure 14. Silica nanoparticle introduction to PAA through (a) ex situ process, and (b) in situ process.	18

List of Figures (Continued)

Figure	Page
Figure 15. Profiles of two spin coating processes measuring speed over time (top), and resulting thickness of the films produced with each method (bottom).	19
Figure 16. Temperature profile of the curing process over time.	20
Figure 17. Two finished PI/SiO ₂ samples, created through ex situ process (left), and in situ process (right).	21
Figure 18. Optical profiles of two samples. Ex situ (top) has a peak to peak range of 2200 nm. In situ (bottom) has a peak to peak range of 400 nm.	22
Figure 19. Avalanche process showing how one accelerated electron (red) can result in many by ionizing atoms (blue).	24
Figure 20. Schematic of treeing theory as a means of dielectric breakdown.	25
Figure 21. Room temperature dielectric testing rig connected to the hipot tester.	27
Figure 22. (a) Schematic of the cryogenic dielectric testing setup, with a zoomed-in view of a PI/SiO ₂ sample between two electrodes, and (b) an image of the electrode holders in the mount.	29
Figure 23. SEM image of the surface of a PA/SiO ₂ composite sample. Silica particles can be seen as dark grey circular masses, with the PA host represented by the lighter grey area.	31
Figure 24. Comparison of dielectric strength of 0-6% PI/SiO ₂ composites at 300 K (patterned red) and 92 K (solid blue).	33
Figure 25. SEM image of a PA/SiO ₂ composite sample containing 4% wt. silica.	35
Figure 26. Number of particles within set diameter ranges. Data gathered from an SEM image of a 6% silica sample.	36
Figure 27. Elemental map of silicon in a 5% wt. PA/SiO ₂ composite sample obtained through SEM-EDS.	37
Figure 28. SEM image of a breakdown point within a 2% PI/SiO ₂ composite sample broken down at 300 K.	39

List of Figures (Continued)

Figure	Page
Figure 29. SEM image of a point of breakdown within a 1% PI/SiO ₂ composite sample, tested at 92 K.	40
Figure 30. Close inspection of the material damaged in a cryogenic dielectric test, using a zoomed-in view of the 1% PI/SiO ₂ sample in Figure 29.	42
Figure 31. Cryocooler set up (a) provided by the Applied Superconductivity team at the NWSCPD, and (b) as a schematic.	45
Figure 32. Paschen's curve, which plots combined values of pressure and distance against breakdown voltage [63].	47
Figure 33. Flow chart of the helium chamber with a valve diagram.	49
Figure 34. SolidWorks rendering of the inner testing chamber, contained within the outer vacuum chamber.	50
Figure 35. SolidWorks rendering of (a) the helium chamber, and (b) the cross-section of both chambers.	51
Figure 36. SolidWorks simulation of the effects of 1520 Torr operating pressure on the (a) deflection of the inner chamber, and (b) stress of the inner chamber.	53
Figure 37. SolidWorks simulation of the effects of 154.45 N weight on (a) the deflection of a single pipe, and (b) the stress of a single pipe.	54

List of Tables

Table	Page
Table 1. Equation used to determine mass of silica.....	15
Table 2. Equations used to determine mass of precursor materials.....	17
Table 3. Comparison of dielectric strength between this and other studies	57

Chapter 1

Introduction

1.1. Naval Ships and HTS Cables

Power generation and transmission are necessities for any technological device or system, Navy ships included. Ships create a unique problem, however, in their requirement to be self-sufficient for extended periods of time while at sea. Power must be generated on board and transmitted to all subsystems on the ship, without the infrastructure that is present for land-based systems, such as the overhead or underground powerlines seen in cities and towns. One of the most critical limiting factors to onboard power generation and transmission is the amount of space. Every square foot on a Navy ship has a purpose, meaning a larger generator and larger cable bundles are not viable solutions to an increase in power requirements. An increase in efficiency has the potential to meet the ever increasing demand for electrical power on Navy ships.

High-temperature superconducting (HTS) cables provide a means of increasing power density by 200-800% from traditional cables [1]. HTS cables contain a core made of a superconducting alloy, or a superconductor. When a superconductor is cooled to a point below its transition temperature, its electrical resistance drops to zero, resulting in 100% power transmission efficiency [2, 3]. The cable core is usually a hollow cylinder, but may be singular or in three phases [4]. In multi-phase cables, each phase is separated by a dielectric layer. HTS cables are commonly cooled using liquid nitrogen (LN_2) which flows around the outer layer of the cable and through the hollow center. An example of a three-phase HTS cable can be seen in Figure 1 [5].

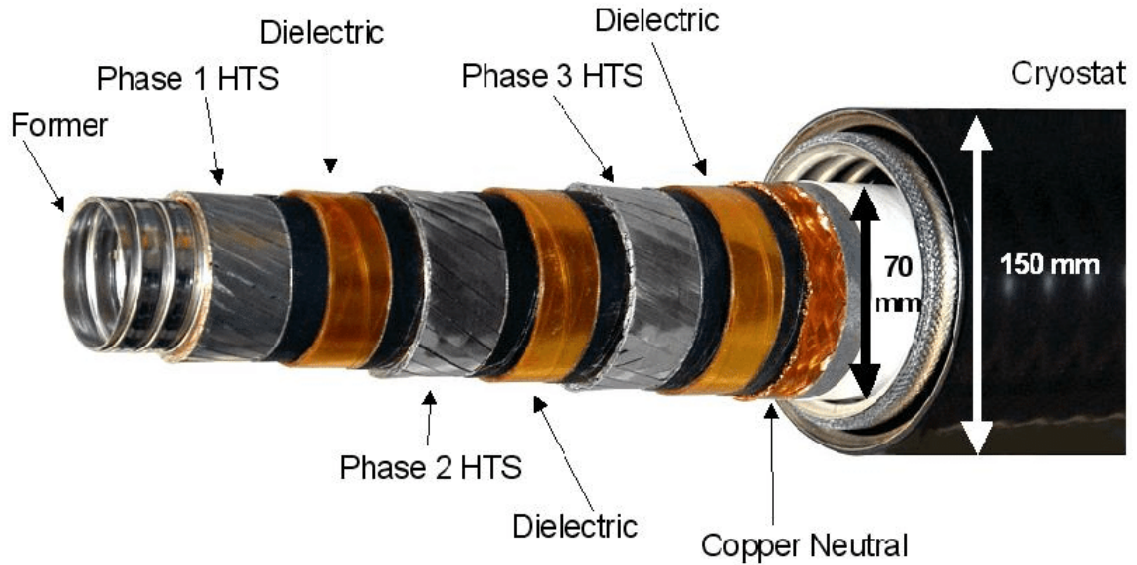


Figure 1. Three phase superconducting cable, with each phase separated by a dielectric, contained within a cryostat [5].

1.2. HTS Cable Applications

HTS cables have a number of potential applications, one of which is a means to increase power transmission on Navy ships while saving space and weight [6]. The increased efficiency associated with these cables can be used on smaller systems, or on a system requiring large amounts of electrical current such as a kinetic energy weapon, commonly known as a rail gun. A rail gun may require as much as 3.4 MA to operate, a current which would require many conventional cables [7, 8]. HTS cables have the potential to transmit the same amount of current more efficiently while using less space.

Navy ships develop a magnetic signature as they travel throughout Earth's magnetic field, a signature that can be picked up by other ships or mines with magnetic triggers [9]. Rather than preventing this magnetic signature from developing, efforts have been made to reduce the signature on ships through degaussing [10, 11]. The process of

degaussing requires the installation of a system of electrical cables along the hull of the ship on both sides, which can be seen in Figure 2 [12]. Running the proper current through these cables results in a magnetic field that cancels out the field output by the ship [13]. Studies have shown that degaussing through HTS cables is not only feasible, but beneficial in terms of weight, size, and cost [12, 14].

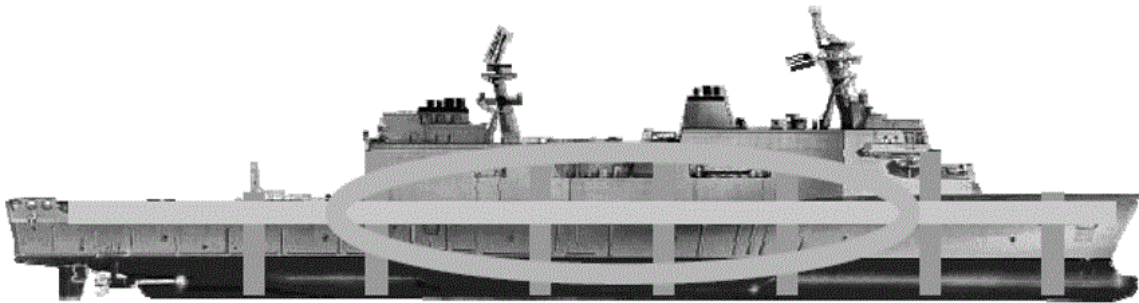


Figure 2. Layout of HTS cables along the hull of a Navy ship. HTS cables are indicated by grey lines running vertically and horizontally [12].

Superconducting cables are also a topic of interest in the electric power industry, as the United States power grid is estimated to lose 10% of all electricity to inefficiencies between the source and the customer [15]. Some HTS cable systems have been in place since as early as 2006. In Albany, New York, a 350 m underground HTS cable was installed within the power grid in one phase of the Albany Cable Project [16]. The cable operated successfully and provided power to over 25,000 homes within its first year, and is still operational [1, 17]. The schematic view of the cable system can be seen in Figure 3 [17]. Systems have also been installed in Asia and Europe, such as in the AmpaCity

Project, in which a 1,000 m HTS cable was installed as part of the distribution network in Essen, Germany [18, 19].

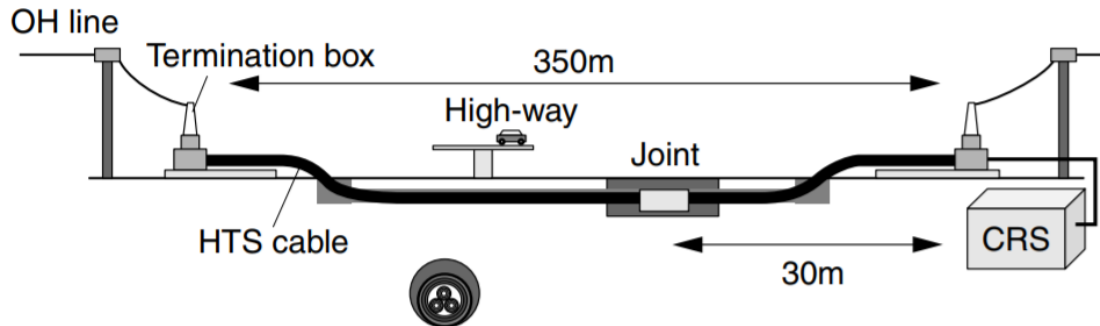


Figure 3. Schematic view of the HTS cable system installed in the Albany Project. The HTS cable runs underground to connect two termination boxes [17].

1.3. Dielectric Requirements

The typical coolant used in HTS cable systems is LN_2 which is capable of reaching anywhere from 64 K to 77 K [20]. However, Naval research has found the ideal operating temperature of HTS cables to be 55 K. This reason, among safety concerns, has prompted Naval research of a purely gaseous cryogen, specifically helium [14]. Helium exists in a gaseous state above 4 K, making it a viable candidate as a cryogen. However, the use of helium as a cryogen results in a new problem. The traditional method of applying electric insulation, lapped dielectric tape, fails when used with a cryogen as permeant as helium. Although the gaps are small, helium atoms are able to move between the laps in the tape, even with multiple layers of dielectric. Helium's ability to permeate the dielectric layers can potentially create a short circuit between different current-

carrying phases, leading to electrical failure of the cable system. An example of this failure is shown in Figure 4. A helium-cooled HTS cable requires a dielectric layer that is impermeable to helium. A common method of coating a cable in another material is polymer extrusion [21]. In the extrusion process, the cable is slowly passed through a bath of liquid polymer. As the cable exits the bath, some of the polymer adheres to the surface, where it remains as it is cured. The cured polymer is one continuous layer with no laps, making it impermeable to a gas [22].

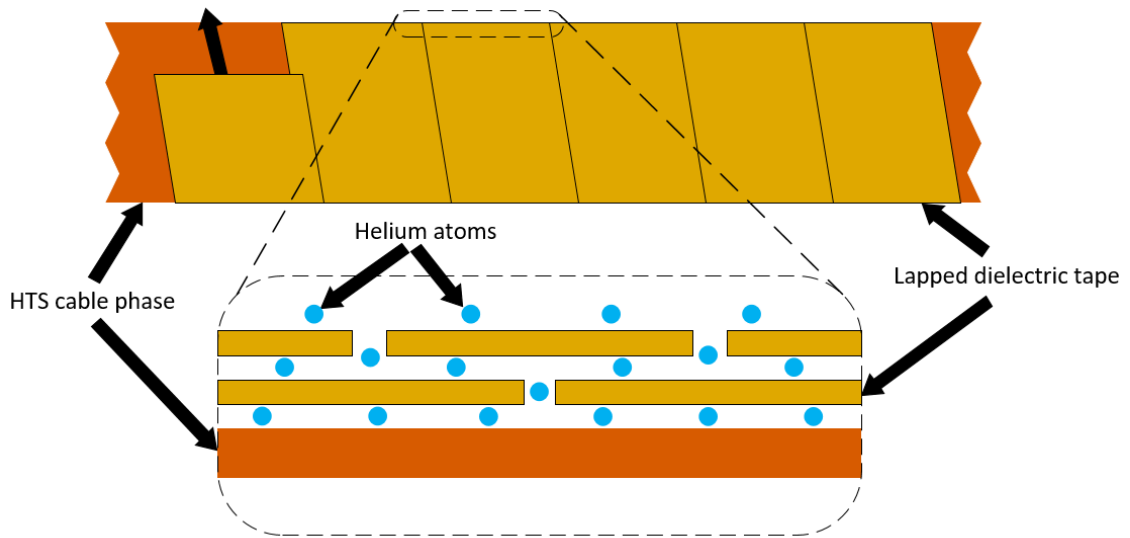


Figure 4. Schematic of helium atoms permeating layers of lapped dielectric tape.

HTS cables transmit large amounts of current, so the insulating material must have sufficient dielectric strength. The HTS cables explored in this research require a dielectric strength of 12 kV/mm. Polymers tend to have dielectric strengths much higher than this requirement, some as high as 300 kV/mm [23]. Although a polymer could be

chosen due to its suitable dielectric strength for an HTS cable, polymers tend to have thermal contraction rates (coefficient of thermal expansion, CTE) much higher than that of the cables in question. Polymers contract at a rate of 0.6-2.7% of their initial length when cooled to 50 K, depending on the material. The HTS cable in question has a rate of contraction of 0.3% in the same temperature range [24]. Contraction rates of common cryogenic materials can be seen in Figure 5 [24]. If an HTS cable was extruded with a pure polymer and subsequently cooled to cryogenic temperature, the polymer would shrink at a much higher rate, leaving parts of the cable exposed or breaking entirely. This difference in contraction rates is demonstrated in Figure 6.

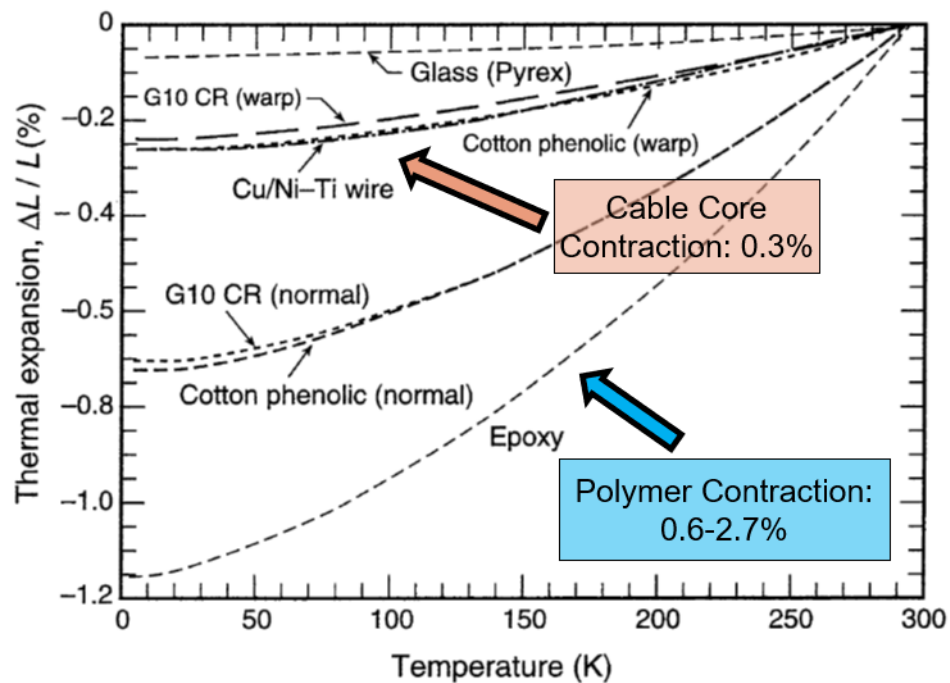


Figure 5. Contraction rates of common cryogenic materials, notably HTS cable cores and polymers [24].

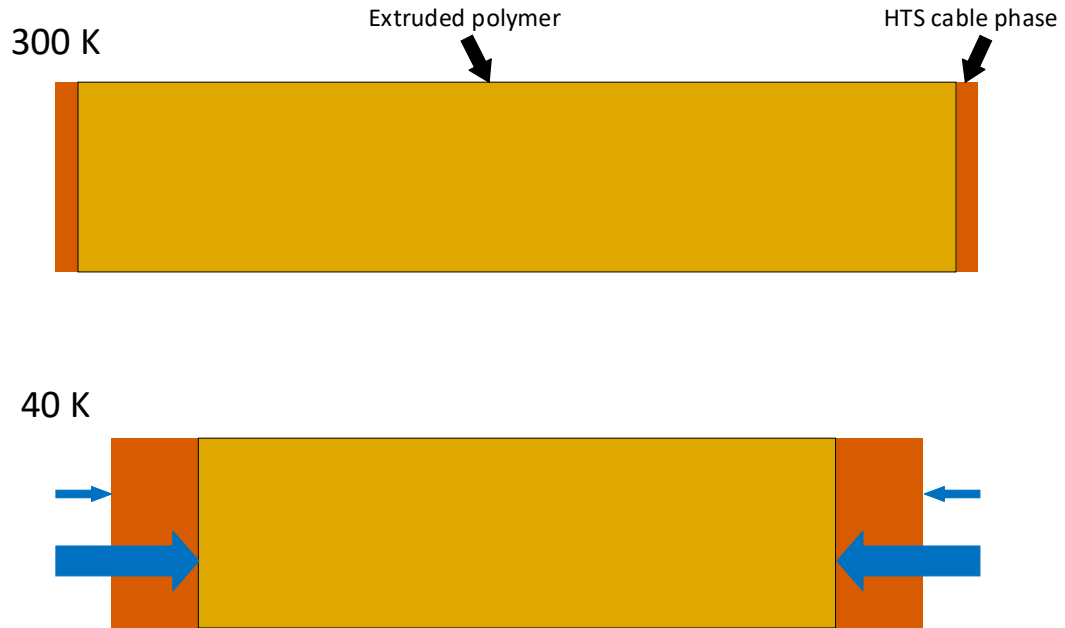


Figure 6. An example of how a dielectric layer with a large CTE could fail when coated on an HTS cable with a lower CTE.

1.4. Nanocomposites

A nanocomposite consists of two phases, the matrix phase and the reinforcing phase. The matrix phase, also known as the host matrix, is the bulk material which contains the reinforcing phase, which in this case is a distribution of nanoparticles. Particles must be smaller than 100 nm in diameter to be considered nanoparticles, and to achieve properties dependent on the high surface area to volume ratio [25]. A diagram of a particle-based nanocomposite can be seen in Figure 7. Nanocomposite materials have been an area of increasing interest since the early 1990s, when researchers found that the addition of nanoparticles to a host material had the potential to greatly improve the host material's physical properties [26]. For this reason, a nanocomposite was chosen to be developed as the dielectric required for a gaseous helium-cooled HTS cable.

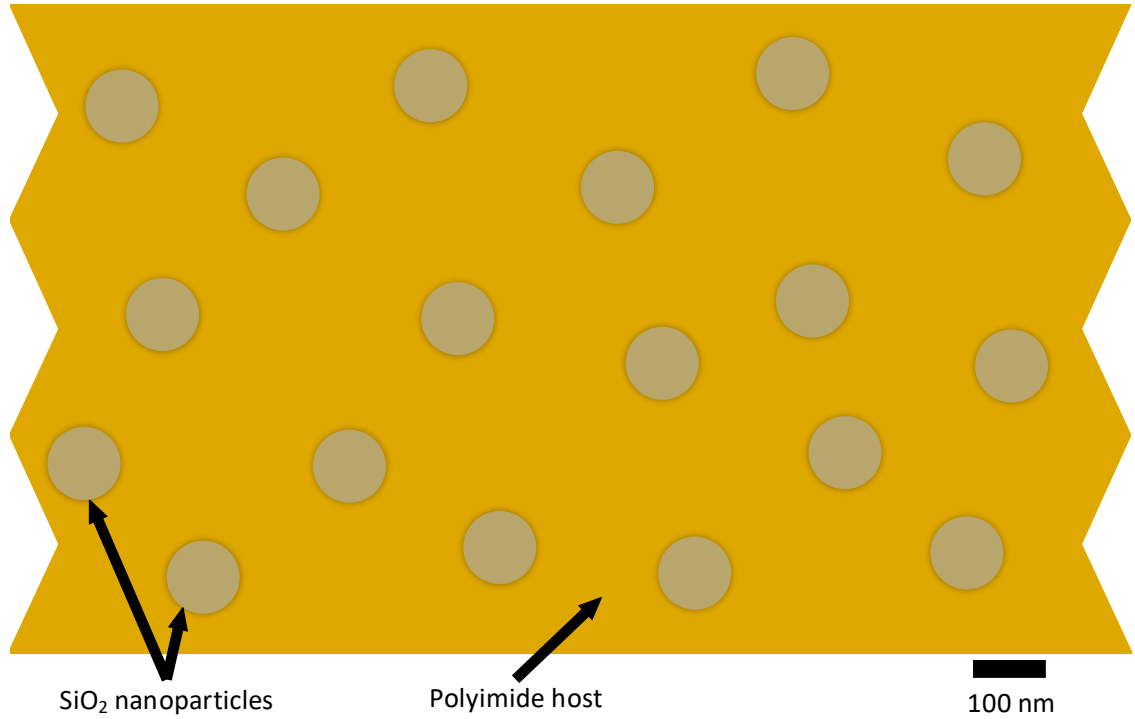


Figure 7. Schematic of a nanocomposite. The host matrix is depicted in yellow, while the nanoparticles are shown in grey.

1.4.1 Host matrix – polyimide. The polymer chosen as the host matrix for this research is polyimide (PI). PI is commercially available in the form of Kapton, developed by DuPont, but Kapton was found difficult to synthesize in a lab setting. Mixing nanoparticles into Kapton was challenging as well. Instead, PI could be generated in-house by converting polyamic acid (PAA) through thermal imidization [27]. The chemical formula for PAA is $(C_{12}H_{12}N_2O \cdot C_{10}H_2O_6)_n$ and its chemical structure can be seen in Figure 8 [28]. PI is a common choice for a dielectric material, with a dielectric strength ranging from 100-300 kV/mm, and a relative permittivity of 3.4 [29, 30]. Further, PI also exhibits excellent flexibility and mechanical strength, and is capable of operating in a wide range of temperatures [31-33]. PI however, like most polymers, has a

high CTE. A nanomaterial with a much lower rate of thermal contraction was chosen to act as the reinforcing phase.

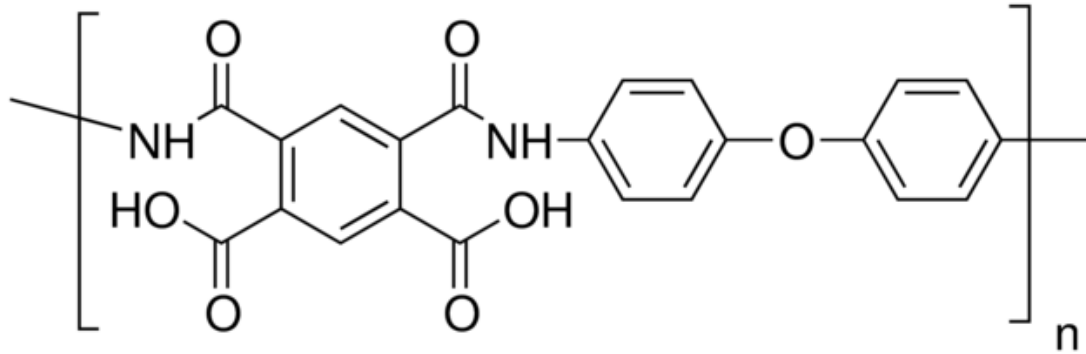


Figure 8. Chemical structure for PAA. The elements present are hydrogen, nitrogen, and oxygen [28].

1.4.2 Nanoparticle – silicon dioxide. The filler material chosen as the reinforcing phase is silicon dioxide (silica, SiO₂). Silica can be fabricated through an in situ process, or purchased and added to the host matrix via an ex situ process, both of which will be explained in detail in Chapter 2 [34, 35]. Purchased silica nanoparticles can be seen in Figure 9. Silica has a thermal contraction rate 15-20 times lower than that of PI [24, 36]. Introducing silica nanoparticles into a PI host matrix could theoretically lower the contraction rate of the composite [37]. Given the proper PI:SiO₂ ratio, it would be possible to match the given CTE of the HTS cable core. The addition of SiO₂ nanoparticles has one notable drawback, as silica has a much lower range of dielectric strength than PI, from 10 – 100 kV/mm, and a relative permittivity of 3.9 [38]. Thus, the

formation of the composite will lower the bulk material's CTE as well as its dielectric strength [39].



Figure 9. Silica particles purchased from Sigma-Aldrich, 20 nm (left) and 80 nm (right) in diameter.

1.5. Cryogenic Testing Chamber

The nanocomposites fabricated throughout this research were tested both at room and cryogenic temperatures. In order to properly characterize the samples for their intended application, they have to be tested in a gaseous helium cryogenic environment. Gaseous helium as a cryogen is a fairly young field of research, and as such there is a limited number of chambers to use as references when designing a new one. Those that are operational exist primarily to cool HTS cables, rather than characterize materials to be used in conjunction with the cables [40, 41]. A diagram of one such chamber can be seen in Figure 10 [41].

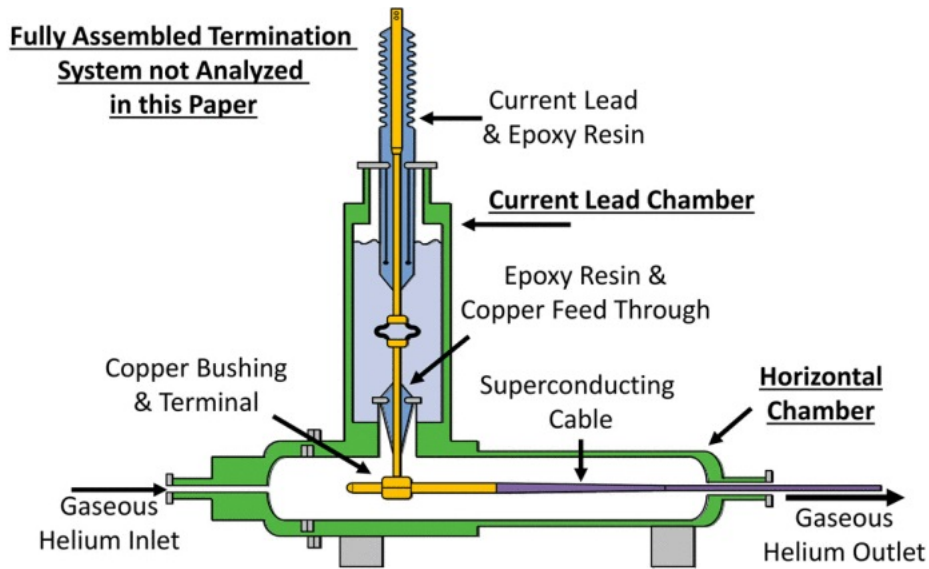


Figure 10. Gaseous helium-cooled cryogenic chamber designed to cool a section of HTS cable [41].

The most feasible option for characterizing the materials fabricated in this research is to do so within a unique chamber designed and built in-house. The testing chamber will fit into a system provided by the Applied Superconductivity Team at the Naval Surface Warfare Center Philadelphia Division (NSWCPD). The testing chamber consists of one compartment, the helium chamber, encased in another, the vacuum chamber. The helium chamber was designed to accommodate dielectric and CTE testing of the PI/SiO₂ composite after gaseous helium has cooled the chamber. The vacuum chamber is built around the helium chamber to provide thermal insulation from outside the system. Given that the ideal operating temperature of the HTS cables is 55 K, the cryogenic chamber is expected to reach as low as 40 K, and use a heating element to control the temperature.

1.6. Motivation and Objectives

In this research the relationship between temperature and physical properties of a polymer nanocomposite are studied, with the hope of creating a dielectric material suitable for use on helium-cooled HTS cables. The properties of the composite can be adjusted due to the rule of mixtures, which uses the concentration of a composite to estimate material properties. HTS cables have been used in recent years, although they used LN₂ as a coolant. In an effort to make these HTS cables even more efficient, a few research groups have explored this topic, but most of the research done here is unique and unprecedented. The motivation of this research is two-fold: to create the dielectric material from a PI/SiO₂ nanocomposite, and to design and fabricate the testing chamber necessary to characterize the composite in a helium-cooled cryogenic environment.

The objectives of this research include:

1. Create a well-dispersed PI/SiO₂ nanocomposite.
2. Perform dielectric tests on composites with varying SiO₂ concentrations to determine which concentrations result in viable candidates for HTS dielectrics.
3. Measure the relationship between temperature and dielectric strength.
4. Design a helium-cooled cryogenic chamber to perform dielectric and CTE tests.

1.7. General Layout of Thesis

In Chapter 2 of this thesis, the two methods used to generate silica nanoparticles are described, as well as the fabrication method of the thin film samples. The quality and

consistency of the two particle generation methods are discussed. The means through which the samples were characterized are described in Chapter 3, including dielectric testing and scanning electron microscopy. The methods for dielectric testing at room and cryogenic temperature are depicted. Chapter 4 contains the results from these tests, in the form of dielectric strength values and SEM images of the samples before and after breakdown. These SEM images are also used in the discussion of the dielectric breakdown theory known as electrical treeing. The design of the helium chamber is detailed in Chapter 5, along with the safety considerations and simulations run on the latest iteration of this design. The paper is concluded in Chapter 6, which contains a summary of all work completed to this point, as well as the future works and goals of this research as it continues into the future.

Chapter 2

Nanocomposite Fabrication

2.1. Nanoparticle Distribution

The PI host polymer was purchased from Sigma-Aldrich in the form of a 15% wt. poly(pyromellitic dianhydride-co-4,4'-oxydianiline) amic acid solution, or polyamic acid ($C_{12}H_{12}N_2O \cdot C_{10}H_2O_6$)_n [28]. The PAA form of the polymer was found to be the easiest to work with in terms of the introduction of nanoparticles, as it is a viscous liquid in this form. It was determined experimentally that 13.8% wt. of the solution remains once fully cured. The difference between the 13.8% wt. experimentally determined and the factory stated 15% is the absence of water in the experimental trials. The change in chemical structure from PAA to PI can be seen in Figure 11 [42]. The imidization process causes PAA to release hydrogen atoms as well as OH groups, resulting in water evaporating from the samples. There were two particle distribution methods explored in this research used to produce samples of 0-6% silica concentration.

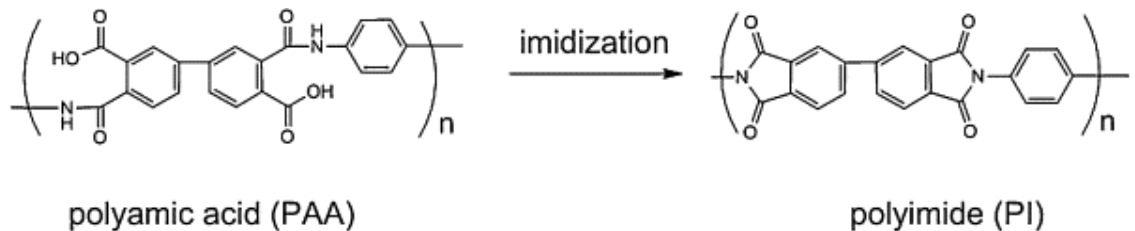


Figure 11. Chemical structures of PAA and PI transitioning through the imidization process [42].

2.1.1 Ex situ method. The ex situ process, or direct mixing process, is the simpler of the two methods. As-purchased SiO₂ nanoparticles, which were 20 nm in diameter, were added directly to the PAA. The mass of the particles (m_{SiO_2}) was dependent on the desired percent concentration (n) and the mass of PAA (m_{PAA}), and determined through Equation (1) in Table 1. Dimethylacetamide (DMAC) was added as a dispersion solvent at a ratio of 15 mL per gram of silica, as it was found to limit the agglomeration of the particles. The silica/DMAC mixture was sonicated in an ultrasonic bath for 30 minutes, which was enough time to create a uniform dispersion [43].

Table 1

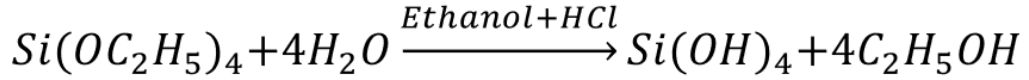
Equation used to determine mass of silica

To determine mass of:	Equation	Number
Silica	$m_{SiO_2} = \frac{n}{1 - n} \times m_{PAA} \times 0.138$	(1)

2.1.2 In situ method. The in situ process begins with four precursor materials being mixed. Ethyl alcohol (EtOH), tetraethyl orthosilicate (TEOS), and hydrochloric acid (HCl) were purchased from Sigma-Aldrich. Deionized water (H₂O) was generated in-house as the fourth precursor. TEOS was purchased with a purity of 98%, and HCl with a reagent percent of 37%. The order of operations which resulted in the most reliable sol gel process consisted of mixing the EtOH and H₂O separately from the TEOS and HCl, then adding these two pairs together. This is done in an effort to eliminate the possibility of water degrading the TEOS and forming a precipitate before HCl is able to

catalyze the sol gel process. Further, adding the TEOS and HCl to the EtOH and H₂O prevents the acid from possibly splashing back, if water was added to the acid.

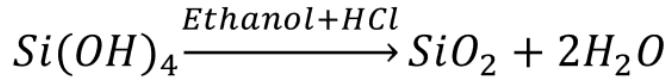
The four precursor materials were set to mix at 350 rpm for 30 minutes, during which time the silica nanoparticles would form through a sol gel process known as the Stöber process [44, 45]. The simplified chemical reactions of the Stöber process can be seen in Figure 12 [46]. The silica particles are generated through multiple steps, including nucleation, growth, aggregation, stabilization, and dehydration. These steps are demonstrated in Figure 13 [47]. This mixing process was found to be exothermic, so the beaker containing the precursors was placed in an ice bath and covered with Parafilm “M” to prevent condensation from the surrounding air. The Stöber process calls for a molar ratio of 1:1:1:2 of EtOH:TEOS:HCl:H₂O, resulting in % wt. ratios of 14.09:63.73:11.15:11.03. The molecular weights of the precursors are 46.07 g/mol, 208.33 g/mol, 36.46 g/mol, and 18.02 g/mol, respectively. Similar to the ex situ process, the masses required of the precursors were dependent on the mass of PAA, specifically the 13.8% that remains after curing. However, the sol gel also undergoes a change in mass when heated. It was determined experimentally that 18.38% wt. of the sol gel remains when cured. Given these values, the sol gel and precursor weights can be determined via Equations (2-6) in Table 2. Schematics comparing the ex situ and in situ processes can be seen in Figure 14. This in situ process is the latest of many iterations, as it was found to produce the most consistent results, in terms of quality of the sol gel as well as the properties of the composite.



Tetraethyl orthosilicate
(TEOS)

Silicon tetra hydroxide
(silicic acid)

Ethanol



SiO₂ nanoparticles

Figure 12. Simplified chemical reactions of the Stöber process resulting in the formation of silica and water.

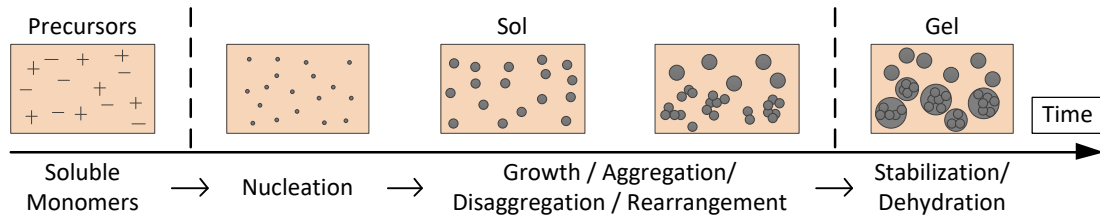


Figure 13. From initial precursors, the steps of nanoparticle formation over time during the sol gel process [47].

Table 2

Equations used to determine mass of precursor materials

To determine mass of:	Equation	Number
Sol gel	$m_{solgel} = \frac{n}{1-n} \times \frac{m_{PAA} \times 0.138}{0.1838}$	(2)
EtOH	$m_{EtOH} = 0.1409 \times m_{solgel}$	(3)
TEOS	$m_{TEOS} = 0.6373 \times m_{solgel}$	(4)
HCl	$m_{HCl} = 0.1115 \times m_{solgel}$	(5)
H ₂ O	$m_{H_2O} = 0.1103 \times m_{solgel}$	(6)

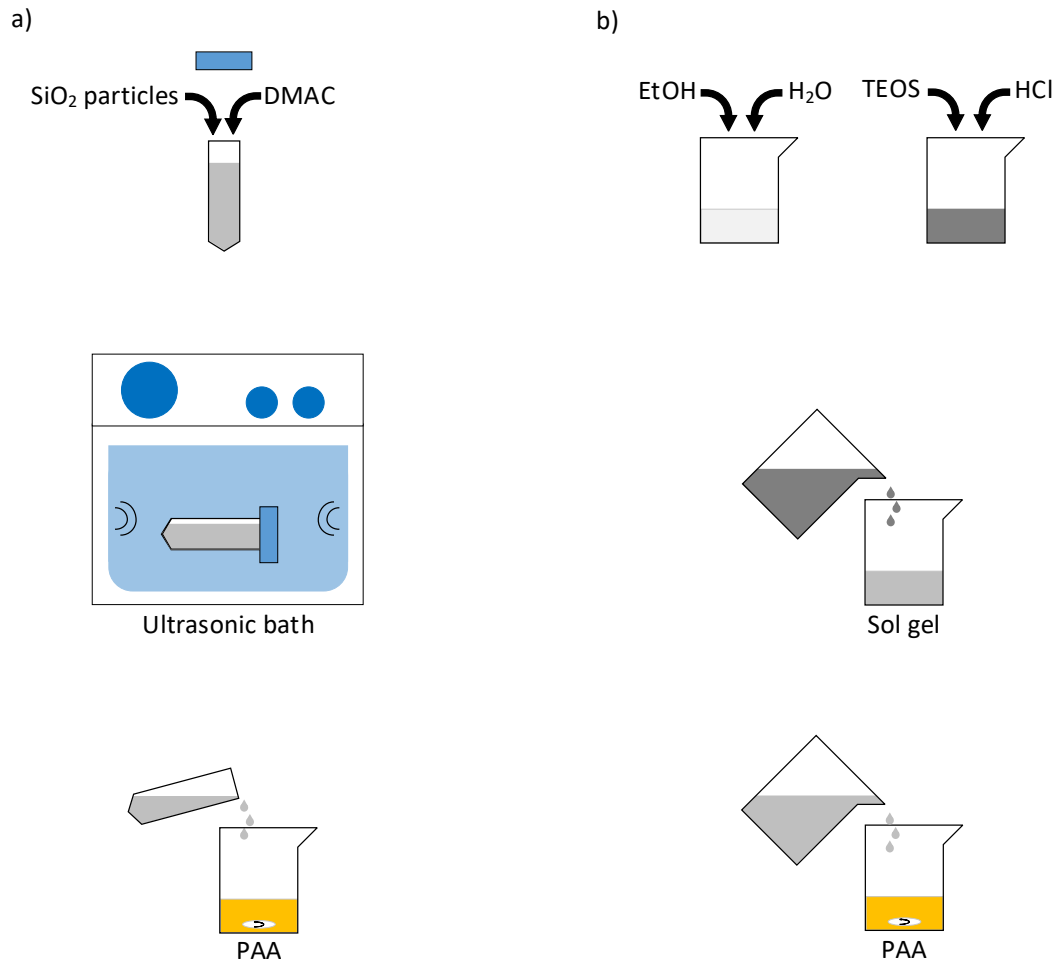


Figure 14. Silica nanoparticle introduction to PAA through (a) ex situ process, and (b) in situ process.

2.2. Thin Film Preparation

The next step in material fabrication is to add the silica particles, whether in the form of a SiO₂/DMAC dispersion or a sol gel, to a beaker containing PAA. This new mixture would mix for four hours at a rate of 50 rpm. Once sufficiently mixed, the silica/PAA mixture was applied to a glass slide to be spin coated. The spin coater accelerates to 1000 rpm over 10 seconds, then remains at 1000 rpm for 45 seconds before

slowing to a stop. The original spin coating method was simply 30 seconds at 1500 rpm, with the maximum acceleration of the spin coater. A comparison of the spin coating profiles over time as well as the resulting thicknesses can be seen in Figure 15. The updated spin coating process was found to be much more consistent in terms of film thickness. Once the spin coating process was completed, the resulting film took the shape of the glass slide it was casted onto, 2.5 cm × 7.5 cm in size, with an average thickness of approximately 20 μm after the curing process was complete.

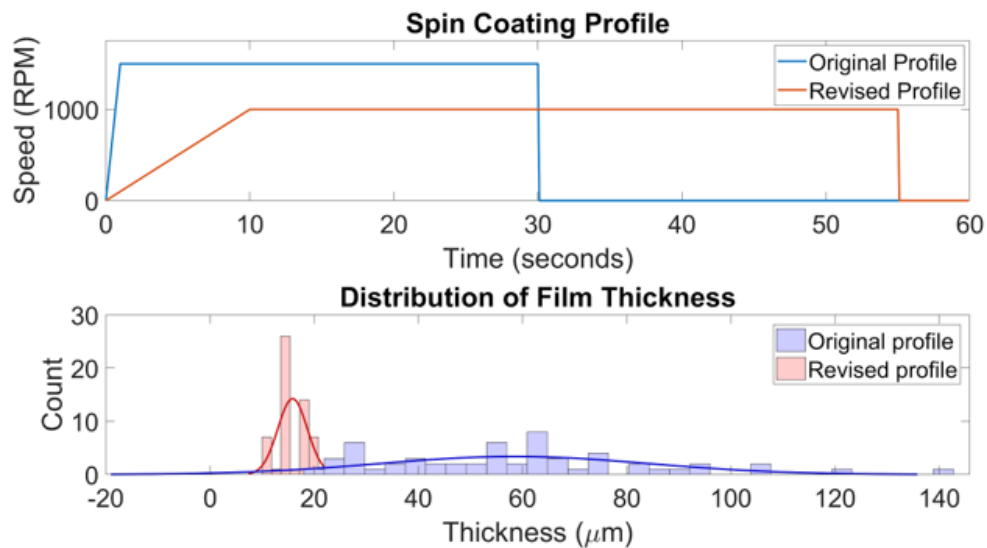


Figure 15. Profiles of two spin coating processes measuring speed over time (top), and resulting thickness of the films produced with each method (bottom).

Curing the PAA solution on a hot plate at 80°C for 30 minutes was found to evaporate the amic acid solution, resulting in a polyamide (PA) film. Following this, the hot plate was increased to 100°C for 10 minutes. The temperature was then increased by 25°C every 5 minutes until 250°C was reached, at which it remained for 30 minutes.

After the 30 minutes, the imidization process was completed, converting PA to PI. Lastly, the hot plate was increased to 370°C for 10 minutes to thermally anneal the sample [48].

The temperature profile of the curing process can be seen in Figure 16.

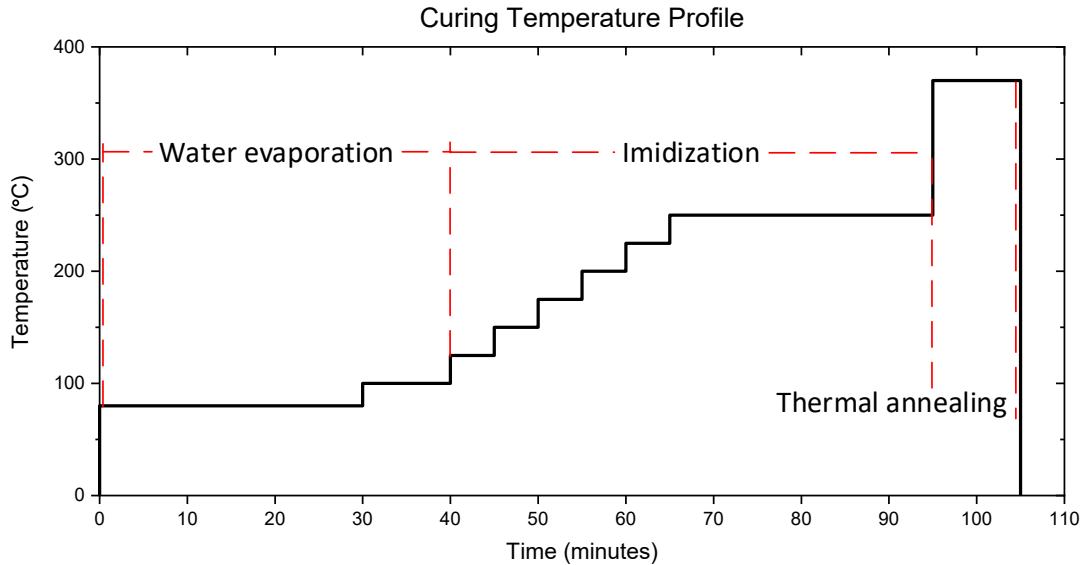


Figure 16. Temperature profile of the curing process over time.

2.3. Discussion of Fabrication Methods

Both the ex situ and in situ methods were successful in the fabrication of PI/SiO₂ thin films. An image showing a finished sample from each fabrication method can be seen in Figure 17. The ex situ sample can be observed to have a matte finish, as it does not reflect as much light and appears duller than the in situ sample. The in situ sample, however, has a much glossier finish, as it reflects more light. This is suspected to be a result of the difference in the surface roughness, caused by silica's higher tendency to

agglomerate in ex situ samples. When the particles group together, they form large inconsistencies within the sample, sometimes affecting the surface. A 3D optical profiler was used to examine the surface roughness of the two 5% silica samples, and the results of these tests can be seen in Figure 18.



Figure 17. Two finished PI/SiO₂ samples, created through ex situ process (left), and in situ process (right).

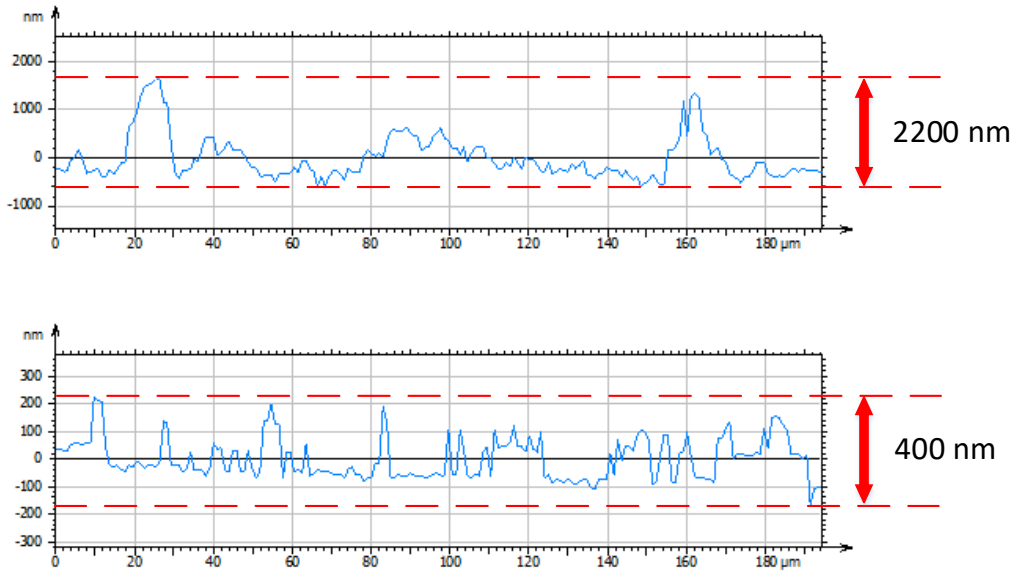


Figure 18. Optical profiles of two samples. Ex situ (top) has a peak to peak range of 2200 nm. In situ (bottom) has a peak to peak range of 400 nm.

The samples created through the ex situ method, as can be seen in the optical profile, have much more variation in surface roughness. Further, the silica in ex situ samples have a greater tendency to agglomerate. As silica has the lower dielectric strength of the two materials being used, an agglomeration is essentially a weak point at which the sample would be likely to fail when placed in a strong electric field. A more uniform dispersion of silica particles would result in an overall higher and more consistent dielectric strength throughout the sample. For these reasons, the in situ fabrication process was found to be more desirable, and the research proceeded with this method.

Chapter 3

Material Characterization

3.1. Dielectric Breakdown Testing

Dielectric breakdown occurs when an electrically insulating material, placed under an electric field, fails and creates a pathway for current to flow [49]. Breakdown can occur in solid, liquid, and gaseous states, as well as in a vacuum. There are varying theories on the mechanism through which breakdown occurs, specifically within solids. One such theory, known as electron avalanche theory, is explored in this research [50, 51]. An electron avalanche functions similar to an avalanche of snow, where one bit of snow builds upon itself, growing in quantity and intensity as it affects more snow around it. A strong electric field may cause free electrons to accelerate within a solid. These electrons are capable of impacting other atoms, causing those atoms to ionize [52]. The ionization of these atoms causes their electrons to accelerate as well, increasing both the number of accelerating electrons and the likelihood of the ionization of other atoms. As this process continues, the number of accelerating electrons grows exponentially until the material experiences dielectric breakdown [53]. A schematic of this process can be seen in Figure 19. The voltage at which this activity occurs is known as its breakdown voltage.

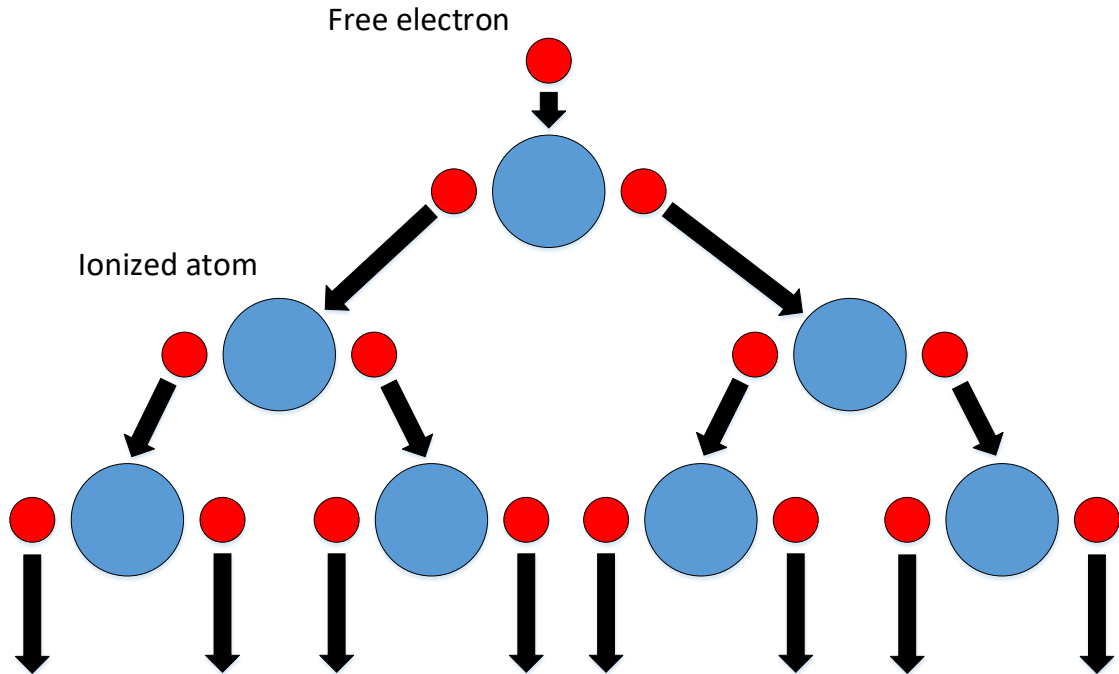


Figure 19. Avalanche process showing how one accelerated electron (red) can result in many by ionizing atoms (blue).

Avalanche breakdown can be paired with the theory of electrical treeing. Treeing theory states that as a solid dielectric nears the breakdown voltage, multiple partial electrical discharges occur throughout the sample [54]. These partial discharges are referred to as tree branches, owing to the manner in which they spread. The breakdown is completed when the first branch reaches a ground, at which point it becomes a tree channel. This tree channel increases in width, and resembles the trunk of a tree [55]. An example of electrical treeing in a solid can be seen in Figure 20.

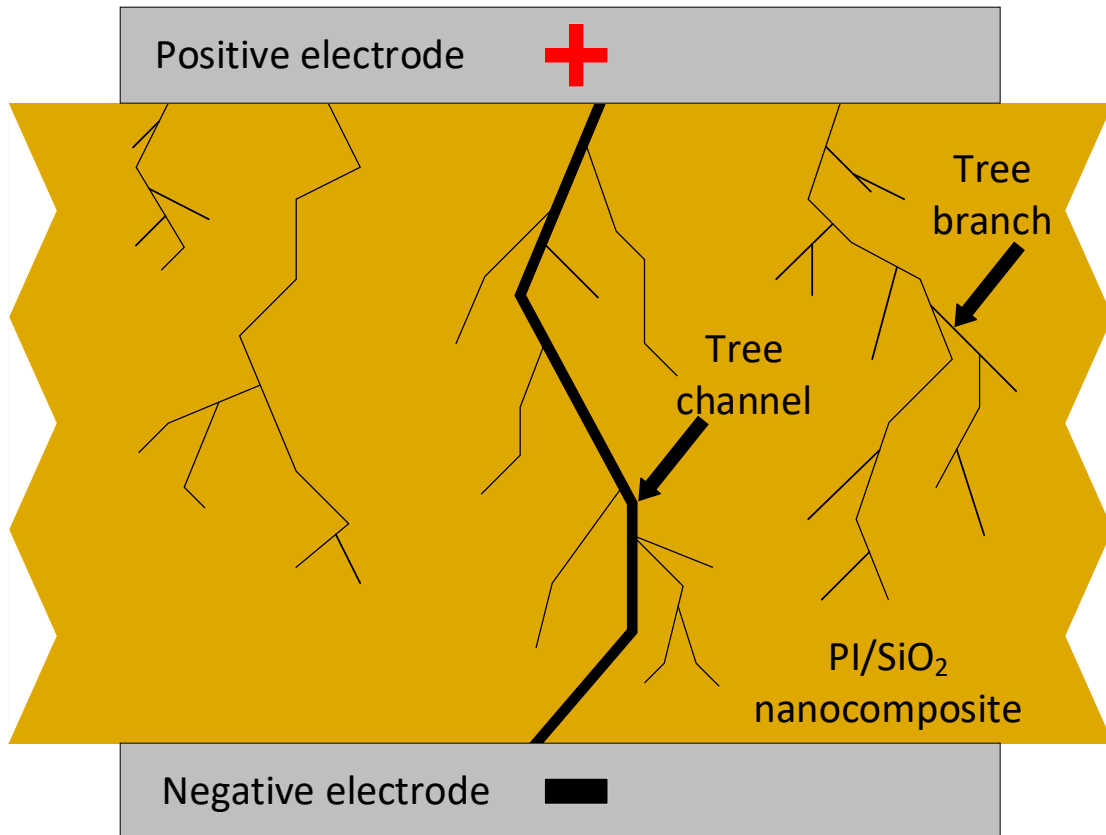


Figure 20. Schematic of treeing theory as a means of dielectric breakdown.

3.1.1 Dielectric testing at room temperature. A fixture suitable for dielectric testing was fabricated in-house, and was designed in accordance with Section 4 of the ASTM-D3755 standard. This standard describes a method of dielectric testing under direct voltage stress. The test was designed to take place between two stainless steel electrodes 6.35 mm in diameter. The electrodes were housed in 3D-printed pieces designed to place 50 g on the sample, per the standard, to ensure good contact. Vertical rails were put in place through the 3D-printed pieces to restrict horizontal movement. The electrodes were connected to a positive and a return lead plugged into a 955i high-potential (hipot) tester, a power supply which was purchased from Vitrek. The voltage

applied across the sample increased at a rate of 500 V/s, until the sample was broken down. Breakdown was detected by the hipot when a minimum of a 5 mA current reached the electrode connected to the return wire, which caused the test to immediately stop. Sample size could vary, but had a minimum of 1.5 cm × 1.5 cm to prevent the current from sparking over. A schematic of the testing fixture connected to the hipot tester can be seen in Figure 21.

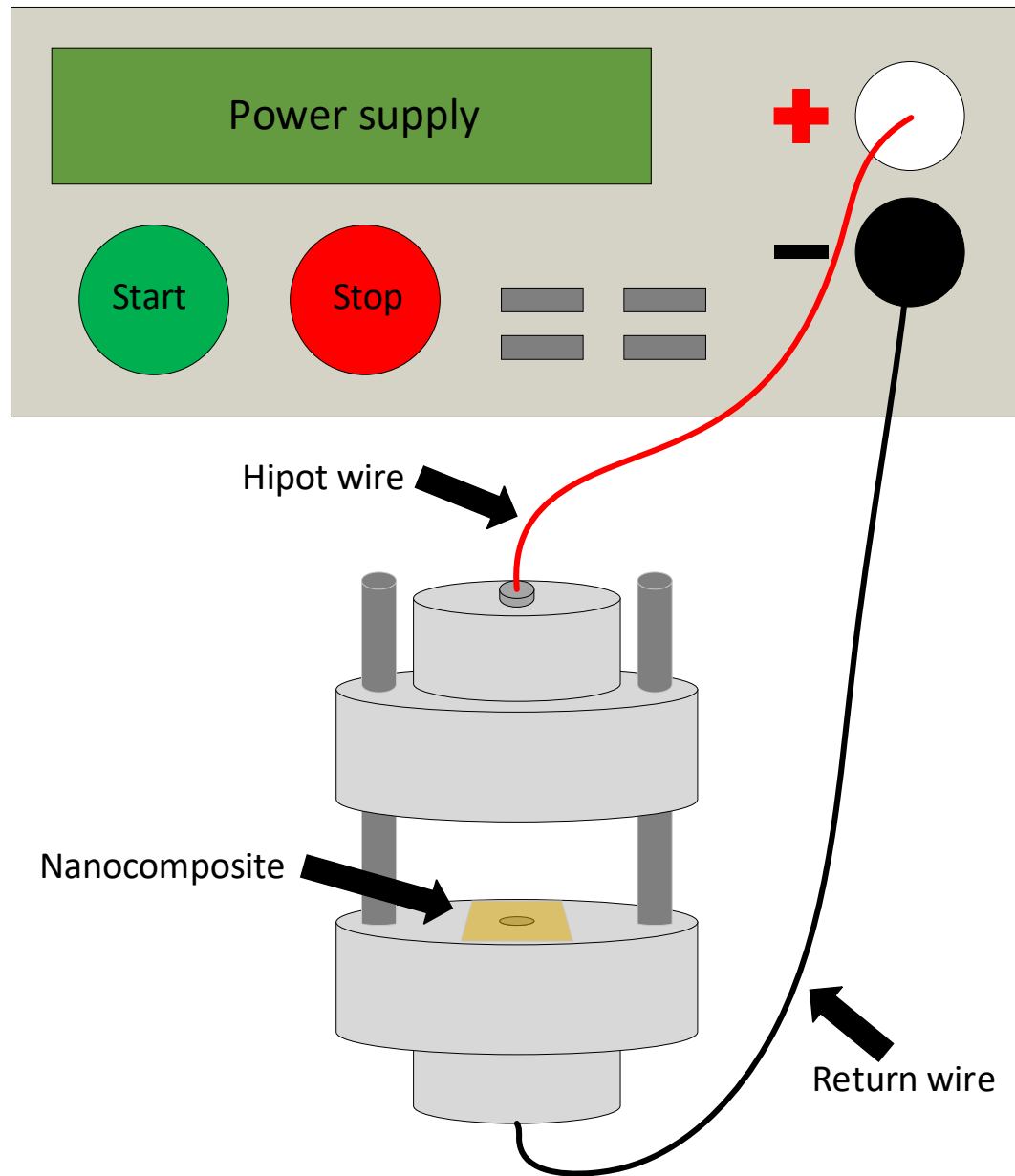


Figure 21. Room temperature dielectric testing rig connected to the hipot tester.

3.1.2 Dielectric testing at cryogenic temperature. Dielectric testing was also performed at cryogenic temperature, however doing so in a helium-cooled environment is not yet possible. Instead, testing was carried out in a dewar containing LN₂. Due to the size of the room temperature testing fixture, a new system had to be designed to fit inside

the mouth of the dewar. The electrodes are housed within Teflon holders, which sit inside of a 3D-printed electrode mount. In an effort to increase efficiency, four electrode pairs were placed inside the mount, allowing for four tests to be run in one cooling cycle. The mount acted as a vertical guide to ensure good contact between the electrodes, and restricted the holders' movement once inside the dewar. A type K thermocouple was affixed to the mount so that the sensor was next to the samples. The mount was attached to a piece of wood long enough to extend out of the mouth of the dewar after the electrodes were lowered. This system, along with the wires, would be lowered into the partially filled dewar until it was just above the surface of LN₂. At the proper height, the samples and electrodes could be cooled to 92 K, a temperature which could be reliably achieved without submerging the samples. The hipot and return wires ran along the length of the wood and plugged into the hipot tester on the outside. However, as the hipot tester could only be connected to one electrode at a time, a switch was placed at the end of the hipot wires. A schematic of this system and a close up of the electrodes in the mount can be seen in Figure 22.

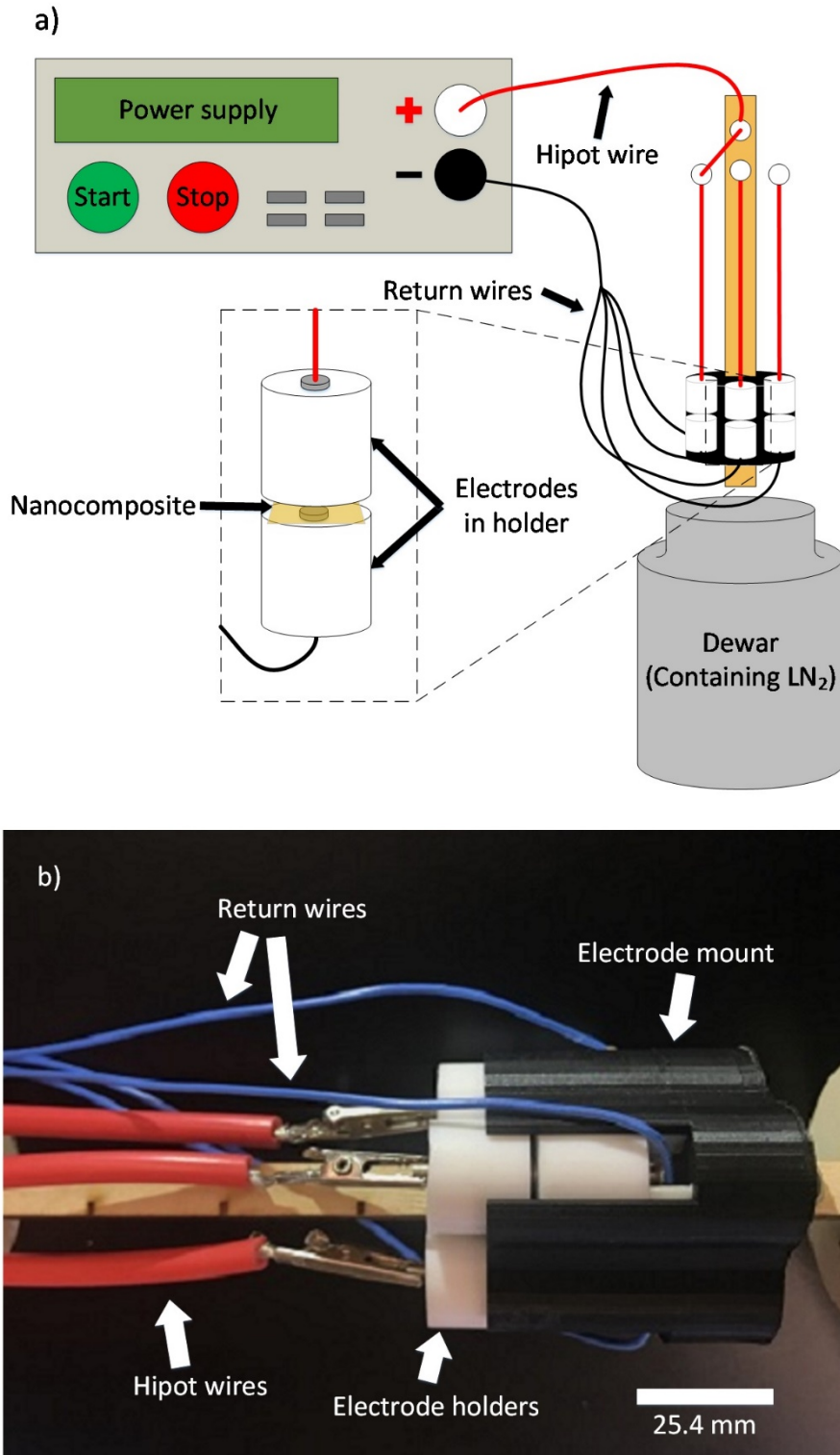


Figure 22. (a) Schematic of the cryogenic dielectric testing setup, with a zoomed-in view of a PI/SiO₂ sample between two electrodes, and (b) an image of the electrode holders in the mount.

3.2. Scanning Electron Microscopy

Samples were imaged on a FEI Apreo scanning electron microscope (SEM) to examine particle size and distribution. All samples imaged on the SEM had to be adhered to a metal stub using carbon tape. The stubs are about 1 cm in diameter, so samples were cut to size as needed. Once the samples were adhered to the stub, copper tape was used to connect the edges of the sample to the metal stub in order to increase conductivity. Due to the nature of the SEM, a more conductive sample has potential to result in a clearer image. The samples were imaged in random areas when checking for particle size and dispersion. One such image can be seen in Figure 23, which shows silica particles dispersed throughout a PA host matrix. Particles were found to be easier to image in a PA host rather than PI, so some samples were imaged before the imidization process was completed. Samples that underwent dielectric breakdown were also imaged on the SEM to examine the points of failure.

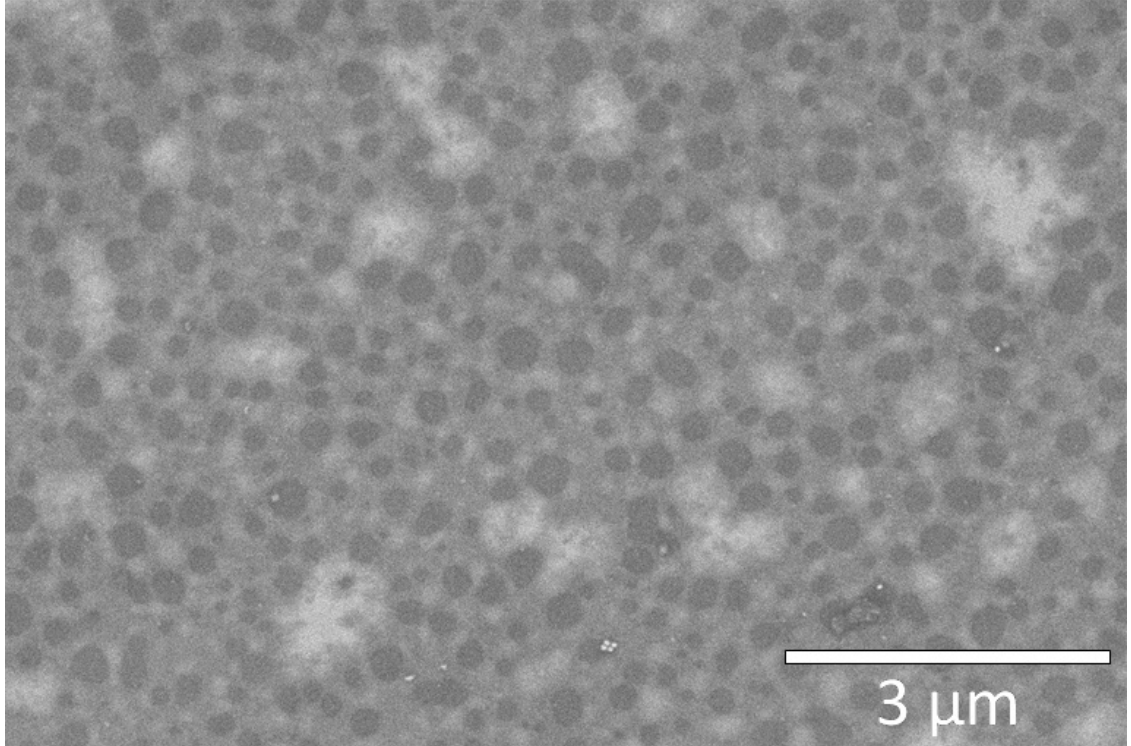


Figure 23. SEM image of the surface of a PA/SiO₂ composite sample. Silica particles can be seen as dark grey circular masses, with the PA host represented by the lighter grey area.

3.2.1 Energy-Dispersive x-ray spectroscopy. Particles were found difficult to image given the insulating nature of the PI host matrix. In an effort to combat this, energy-dispersive x-ray spectroscopy (EDS) was used in tandem with the SEM. The EDS system provided a means of examining the particles embedded deeper in the host matrix than the SEM alone, which showed mostly surface-level particles. The EDS system was capable of isolating singular elements in a material within the imaged area. In the case of the PI/SiO₂ composites, silicon could be selected as the material to be examined, as it was present in silica but not in PI.

Chapter 4

Characterization Results

4.1. Dielectric Strength

Samples with silica concentrations ranging from 0-6%, along with the control material Kapton, were tested for dielectric strength at 300 K and 92 K. A graph depicting these results can be seen in Figure 24. The dielectric strength of samples tested at room temperature can be seen in the striped red bars. Pure PI and 1% PI/SiO₂ samples exhibit a strength of about 275 kV/mm and 250 kV/mm, respectively. Samples with a 2-6% filler experienced a drop in dielectric strength, averaging around 150 kV/mm at room temperature. This trend has been seen in previous works and is expected, as there seems to be an upper limit to the nanofiller concentration [29]. Above this limit, the effect that silica has on dielectric strength becomes more apparent [56]. Samples of higher concentrations were initially explored, but were found to contain a non-uniform dispersion of silica particles. These large pockets of agglomerated particles resulted in dielectric strengths that varied greatly across a single sample, as well as on a per-sample basis.

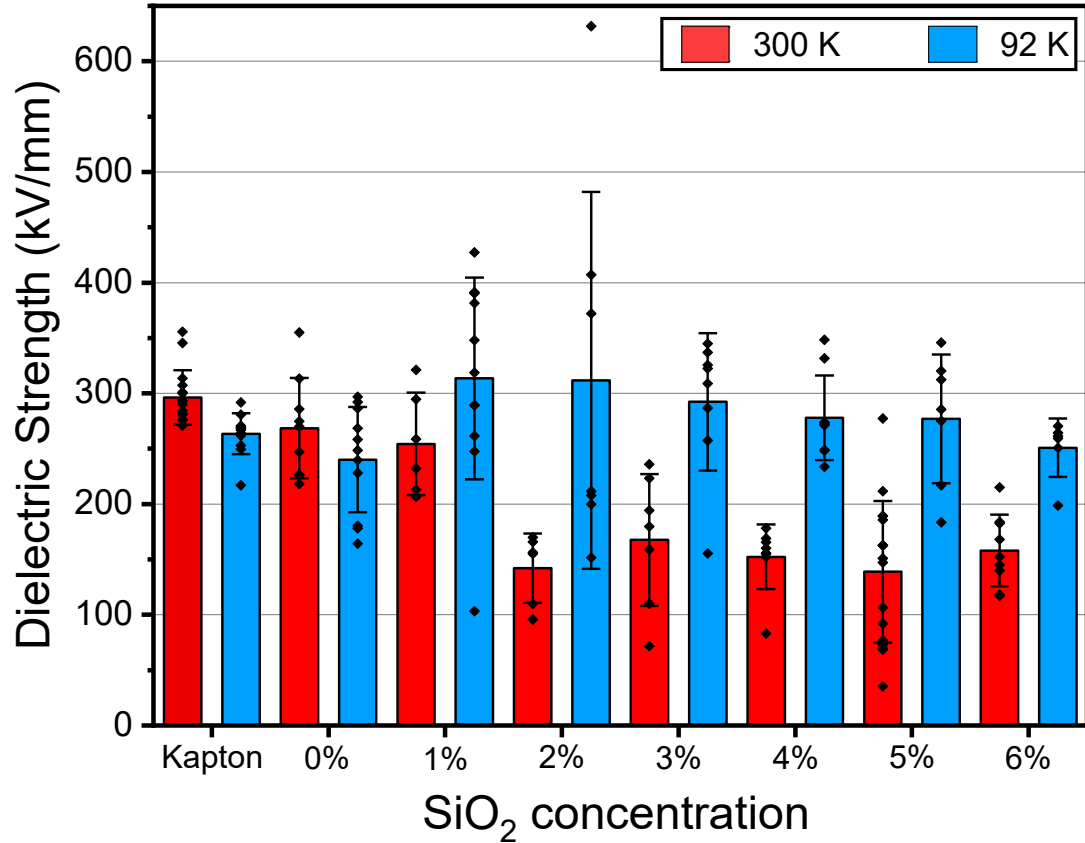


Figure 24. Comparison of dielectric strength of 0-6% PI/SiO₂ composites at 300 K (patterned red) and 92 K (solid blue).

The dielectric strength of samples tested at cryogenic temperatures can be seen in the solid blue bars of Figure 24. Contrary to the room temperature samples, these show an increase in dielectric strength as silica particles are introduced. Whereas pure PI showed a strength of about 275 kV/mm, lower concentrations yielded a strength of over 300 kV/mm. This strength decreased as filler concentration was increased to 6%, but was never significantly weaker than pure PI at 92 K. All composite samples showed an increase in dielectric strength ranging from around 75-150 kV/mm when cooled. This rise in strength is due to the shrinking of the transition layer between the silica particles and

host matrix, owing to the difference in their thermal contraction rates. The change in temperature results in the PI matrix shrinking at a much faster rate than the SiO₂ particles, causing the host matrix to increase in density and tighten the transition layers around each nanoparticle. This increase in density limits the electron paths when the sample is under strong electrical stress. This in turn results in the increase of the voltage required to achieve breakdown [57].

4.2. SEM Imaging

Composite samples were imaged on an SEM to examine particle diameter and distribution. However, due to the insulating nature of PI, the particles proved difficult to image. To circumvent this issue, particles were imaged in a PA host which was not fully cured. There is no change made to the particles during the imidization process, so it is assumed that particles in a PI host are identical to those in PA. One such composite of 4% concentration can be seen in Figure 25. The silica particles are the circular objects within the grey PA matrix. Size of these particles varies in diameter from about 100 nm – 1 μm, but in previous studies it has been found that the majority of particles are less than 200 nm in diameter [47]. A MATLAB code was used to count the number of silica particles within a set area of a sample, and measure their diameter. The compiled data from a 6% concentration can be seen in Figure 26, along with the sample that the measurements were taken from. The chart counts the number of particles within 100 nm increments. Out of over 700 measured particles, about 350 were found to have a diameter less than 100 nm. The variation in particle diameter is a result of the method of their formation, as depicted in Figure 13. The particles grow over time throughout the sol gel process, but

not all particles undergo nucleation at exactly the same time. An extension of this work could be focused on particle size control, which would help us fabricate samples with greater particle size consistency or provide insight to how the particles are affected by different aspects of the sol gel process. While the size varies, the distribution of the particles appears consistent throughout the sample, resulting in a dielectric with no obvious weak points.

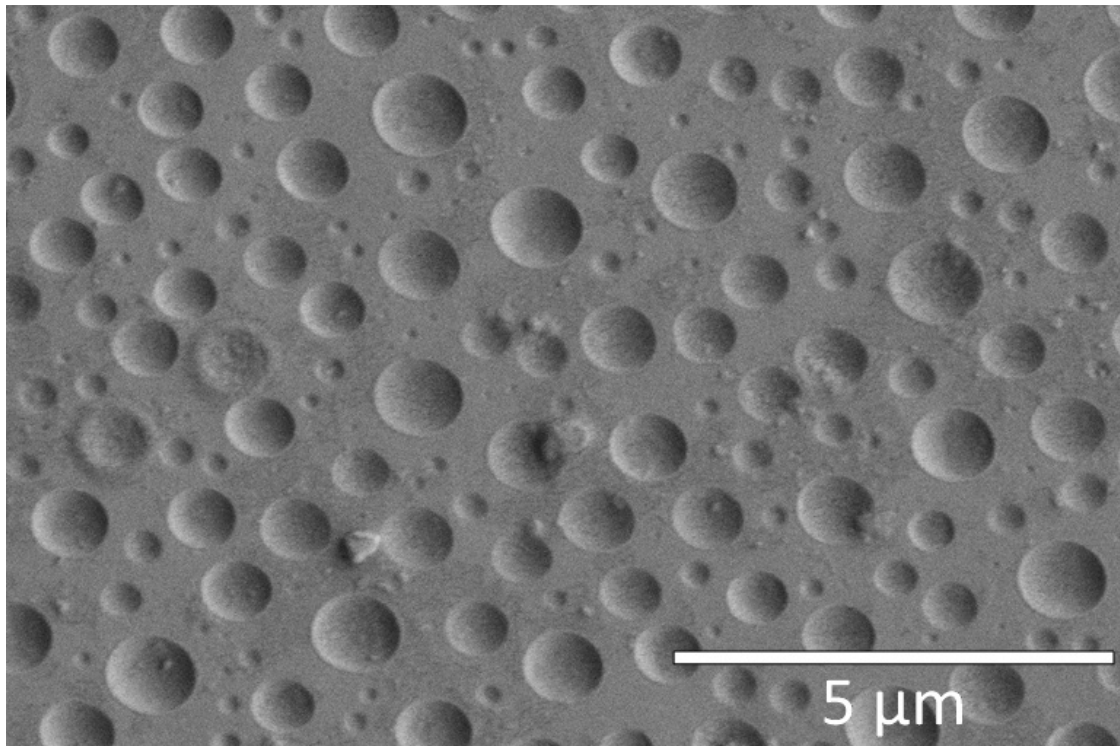


Figure 25. SEM image of a PA/SiO₂ composite sample containing 4% wt. silica.

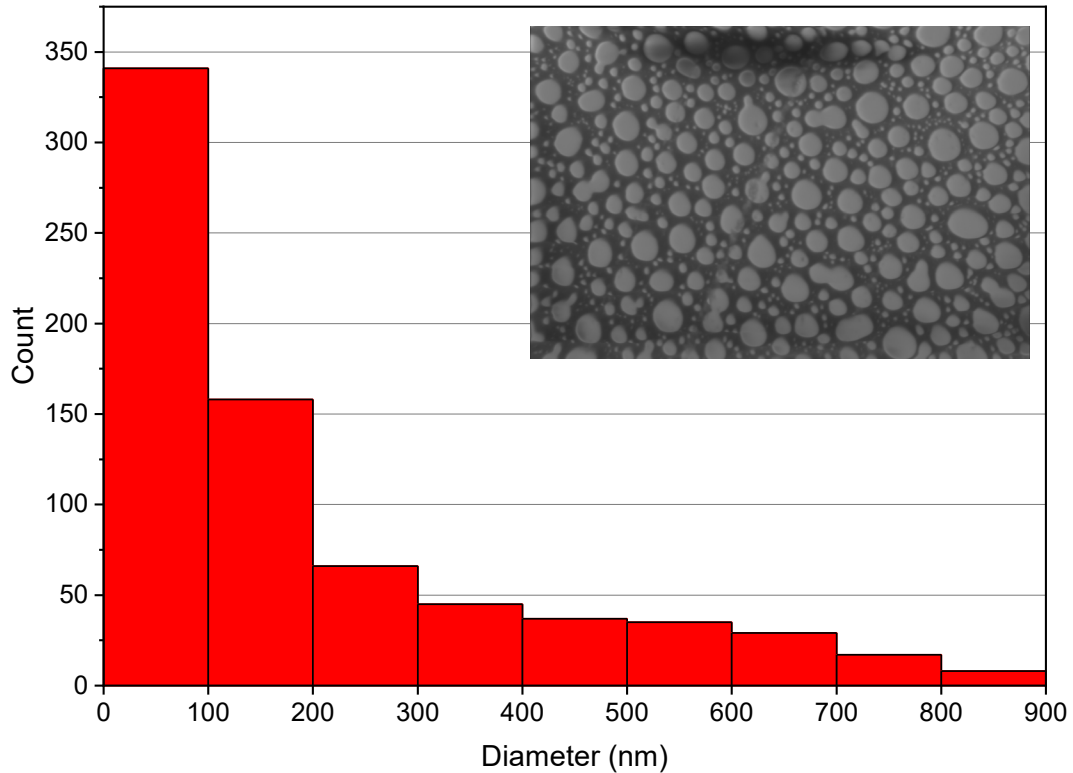


Figure 26. Number of particles within set diameter ranges. Data gathered from an SEM image of a 6% silica sample.

4.2.1 EDS imaging. EDS was used in tandem with the SEM to better image the silica particles, and to confirm that the circular objects seen in the images are indeed silica. By isolating silicon, the EDS system was able to obtain the image shown in Figure 27. The sample used in this image is a 5% silica sample in a PA host. Any area containing red depicts the location of silicon. As the red areas are separate and circular, it can be concluded that the SiO_2 particles remain intact and do not tend to agglomerate. Some particles appear darker red and seem to overlap with others, but these particles are

actually beneath the bright red particles. The layer of PA between these particles and the surface is represented by the black space seen throughout the image.

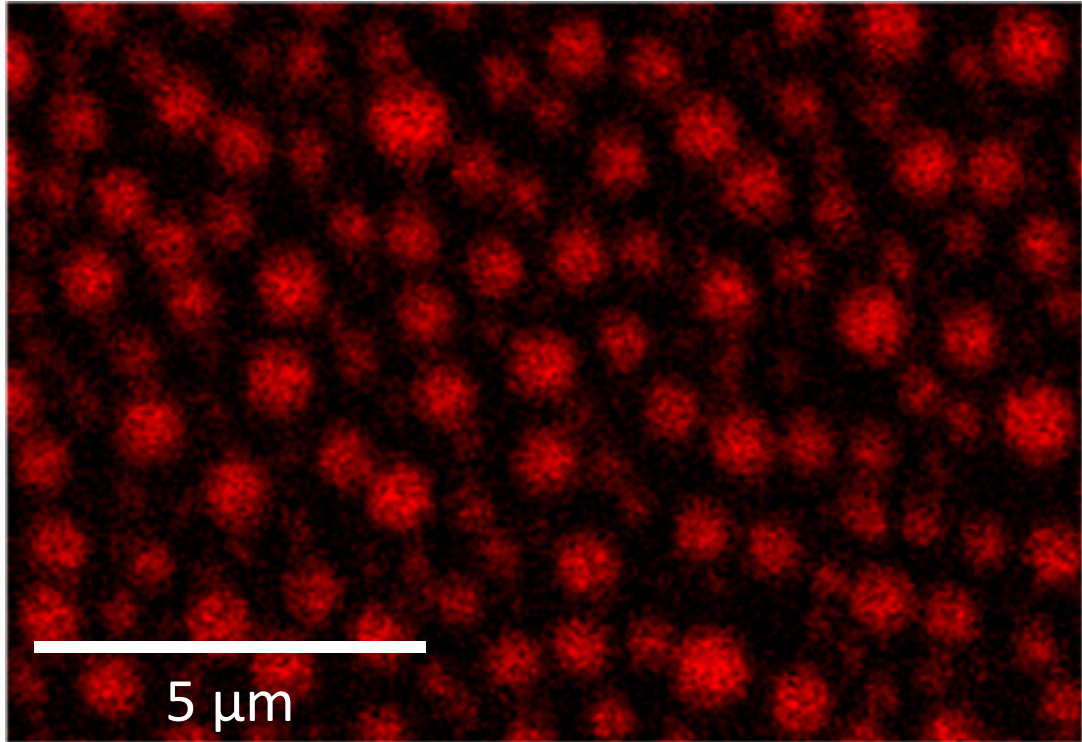


Figure 27. Elemental map of silicon in a 5% wt. PA/SiO₂ composite sample obtained through SEM-EDS.

4.3. Breakdown Point Imaging

The SEM was also used to image samples that underwent dielectric breakdown, as a means of examining the point of failure. Samples broken down at 300 K and 92 K break down through the same mechanism, however the geometric characteristics of the points of failure differ depending on the temperature at which breakdown occurred. An

SEM image of a 2% PI/SiO₂ sample broken down at room temperature can be seen in Figure 28. PI samples were no longer difficult to image after breakdown, as the point of failure provides a direct route to the carbon tape, resulting in a clearer image. The breakdown point is the large black area in the center of the image. As there is no material remaining at that point, electrons are not reflected back to the detectors in the SEM. This breakdown hole is roughly 50 μm in diameter. The area surrounding the hole is damaged during the test, and is shown in the SEM image as the textured grey circumference around the hole. This area appears higher than the material around it, as if it was bunched up as the hole expanded. The remainder of the image is simply material that did not fail. All samples that were imaged after room temperature tests showed similar breakdown structures.

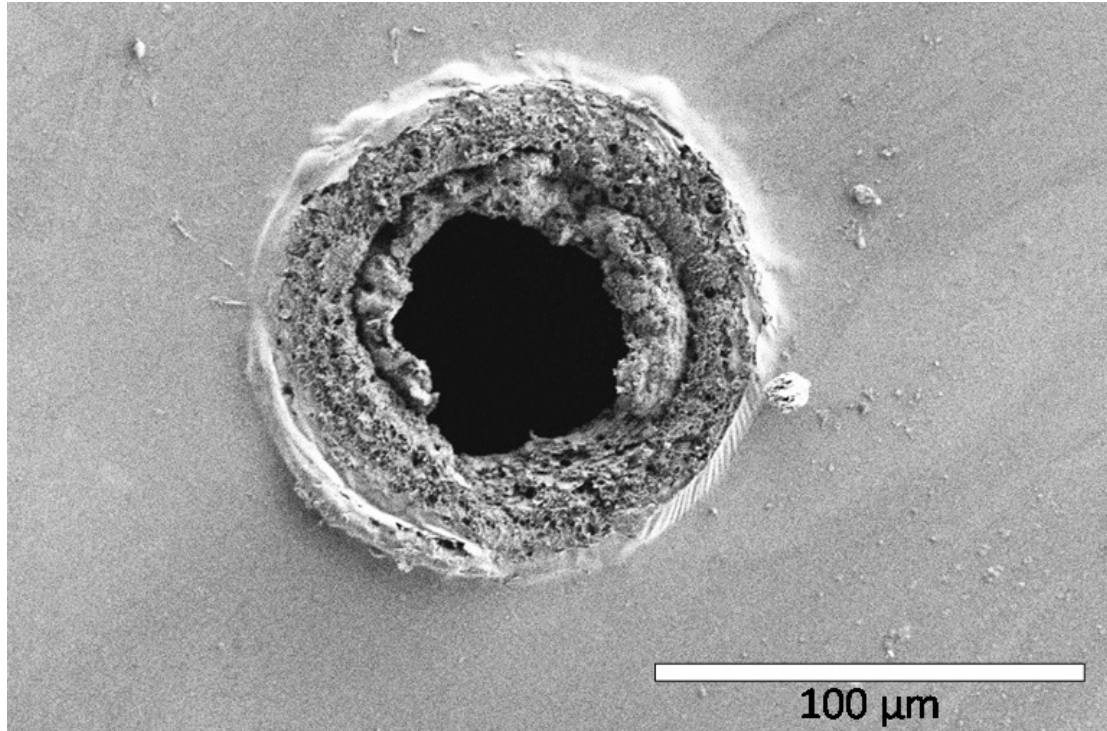


Figure 28. SEM image of a breakdown point within a 2% PI/SiO₂ composite sample broken down at 300 K.

Samples tested at 92 K exhibited differences in the points of failure, despite undergoing the same failure mechanism. A 1% PI/SiO₂ sample broken down at 92 K can be seen in Figure 29. The dark area in the middle is still the point of breakdown, but notably there is not one large through hole. In the case of all cryogenic breakdown samples, the material remains within the area of breakdown, unlike those tested at room temperature. During the tests, the composite has a tendency to store energy produced by the strong electric field. This energy storage can generate heat within the silica particles and the PI host. It is possible for this generated heat to surpass the glass transition temperature of the PI, which can lead to localized melting of the polymer between the electrodes. As the melting becomes more severe, the localized melting area begins to

grow, forming a large amorphous area [58]. It is this large amorphous area that causes the through holes seen in samples tested at 300 K.

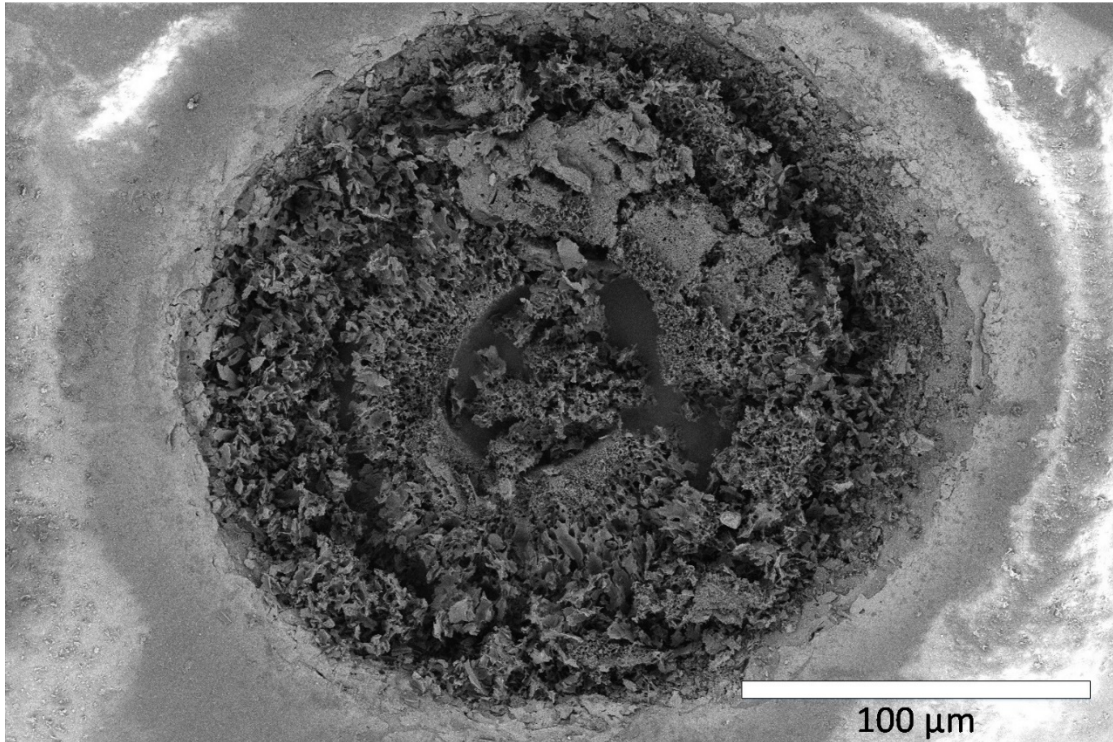


Figure 29. SEM image of a point of breakdown within a 1% PI/SiO₂ composite sample, tested at 92 K.

The localized heating resulting from the strong electric field is present in samples tested cryogenically, but the cold environment inhibits the polymer's tendency to exceed the glass transition temperature. Therefore, in a cryogenic environment, PI can break down while remaining solid [59]. The lower starting temperature of the PI results in a higher energy and heat requirement to reach the glass transition temperature, a requirement which the hipot cannot meet. Additionally, the cryogenic environment

allows for the heat generated within the sample to dissipate rapidly. As a result of these factors, samples broken down at cryogenic temperatures exhibit different breakdown geometries, specifically the lack of a through hole at the point of failure.

4.4. Evidence of Treeing in Broken Down Samples

During the dielectric breakdown of a solid and composite dielectric, the particles embedded in the host matrix begin to experience partial discharge damage [60]. These partial discharges extend to connect between particles, forming what are known as tree branches. As this continues, eventually one tree branch extends from the charged electrode to the grounded electrode. At this point the branch expands to a wider diameter, becoming the tree channel, this is the through hole seen in most dielectric failures. Samples broken down in a cryogenic environment, since their breakdown points remain intact, provide a means of imaging the tree branches and channel.

The characteristics of treeing can be seen in Figure 30, an SEM image of a 1% silica sample. This is the same sample seen in Figure 29, but shows a zoomed-in section of the same point of breakdown. The tree channel is located in the top-left corner of the image, and is denoted by the dark grey area, which extends through the depth of the sample, revealing the carbon tape below it. The smaller tree branches can be seen all around the tree channel, as they are the small black holes found in the lighter grey of the composite. A few of the tree branches have been circled in Figure 30.

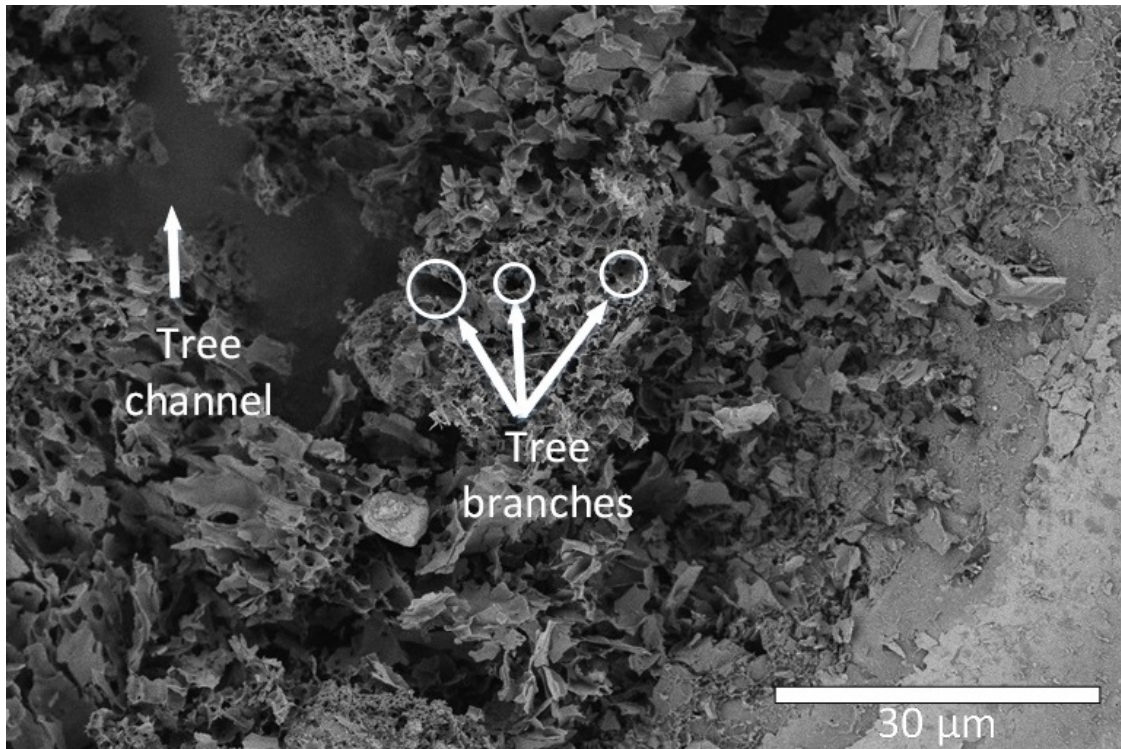


Figure 30. Close inspection of the material damaged in a cryogenic dielectric test, using a zoomed-in view of the 1% PI/SiO₂ sample in Figure 29.

Chapter 5

Cryogenic Testing Chamber

5.1. Design Considerations

The helium chamber's primary goal is to cool samples and equipment to 40 K, so that testing can be carried out in a cryogenic environment. The first factor to be considered for any design is safety. In the case of a helium-cooled cryogenic chamber, safety can be broken up into four categories: pressure build-up, gas leaks, electrical discharge, and temperature exposure. Pressure build-up can occur when a gas is being fed into a chamber, but fails to exit into the larger system. According to ASME standards, the maximum stress that is exerted during a pressure vessel's operation should not exceed 2/3 of the yield strength of the material [61, 62]. Gas leaks most often occur at a joint where two materials meet, usually either with a weld or a flange. There are tools used to detect trace amounts of gas, such as a helium sniffer. If the chamber is filled with helium, the helium sniffer can be used around the outside of the chamber to detect any leaks in the system. Electrical discharge is largely accounted for in the dielectric testing rig, but in the case of its failure, the entire chamber can be grounded. This can be as simple as connecting a wire to the chamber which plugs into the ground prong of an electric socket. Finally, to satisfy any concerns regarding temperature exposure, the chamber containing the cryogenic environment will be encased in a vacuum jacket and have limited penetrations leading to the outside environment. These efforts will work to minimize the amount of convective and conductive heat transfer. Further, any persons near the chamber will wear cryogenic gloves and exercise caution during operation.

The helium cooling and circulation systems were provided for this research by the Applied Superconductivity Team at the NSWCPD. Only the chamber in which the dielectric and CTE testing remains, as can be seen in Figure 31. The Turbo Lab tabletop vacuum pump was purchased from Leybold GmbH, and the helium canister was purchased from Airgas. The cryocooler provided has input and output cryogenic transfer hoses, which end in male bayonet fittings. Therefore, in order to work with the provided system, the test chamber must have input and output female bayonet fittings. These fittings are the only restrictions that the existing system placed on the test chamber. The fan, which is located on the cryocooler, is capable of spinning at a rate of 300 Hz. However, many factors of the cryocooler are unknown, so the mass flow rate of the system is uncertain.

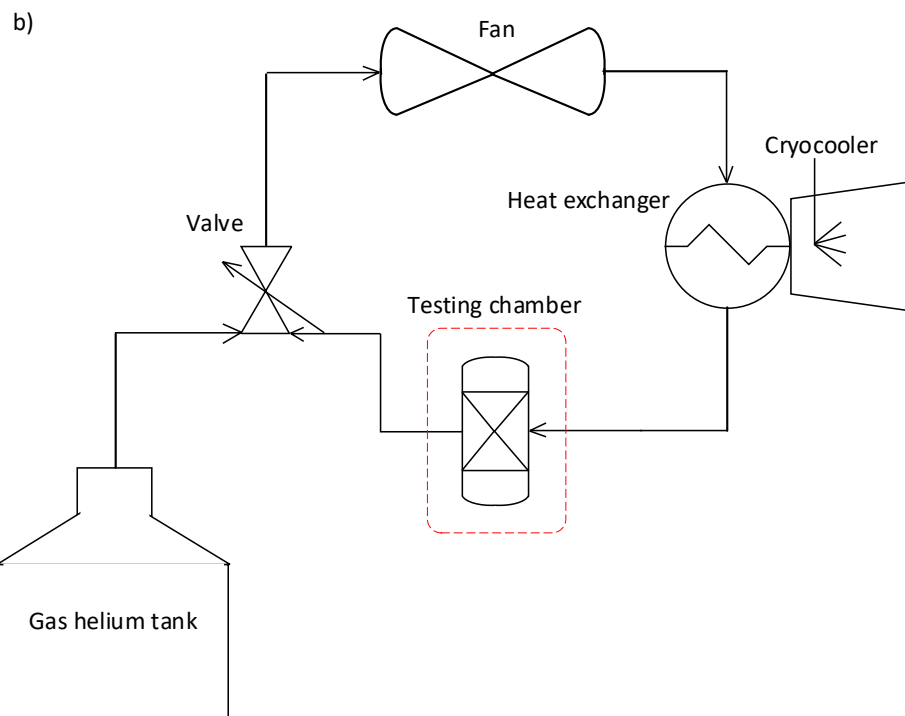
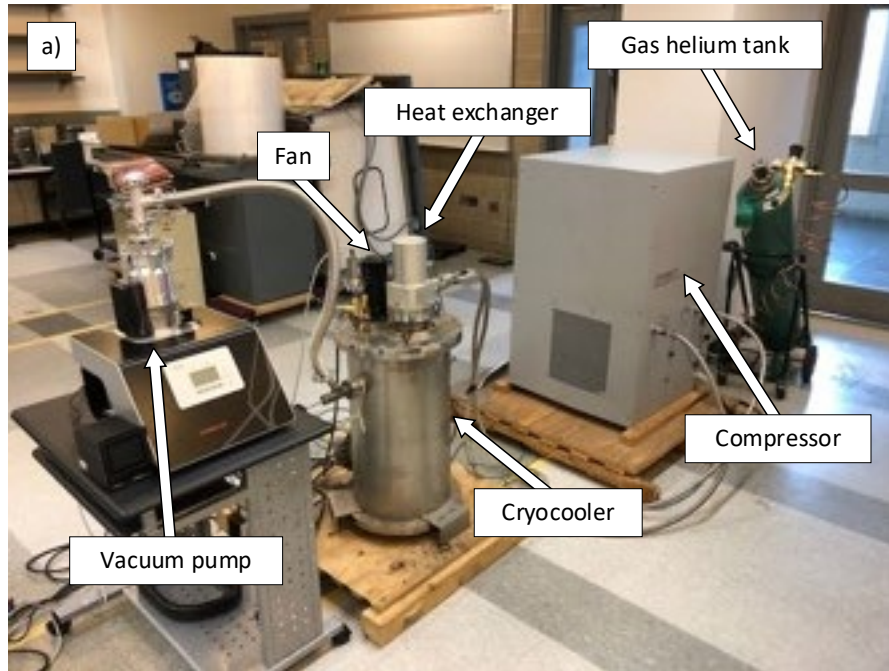


Figure 31. Cryocooler set up (a) provided by the Applied Superconductivity team at the NWSCPD, and (b) as a schematic.

The final consideration involves the pressure of the cryogenic environment, although not just for purposes of yield strength. Operating pressure is a key concept in Paschen's Law, which relates the ambient pressure in a system and the dielectric strength of the material, given the distance between two electrodes. Paschen's curve can be seen in Figure 32 [63]. As the dielectric strength of gaseous helium is at a minimum around 5 Torr·cm, it is imperative to avoid this region. Given the sample size of 1.5 cm × 1.5 cm, thickness of 0.002 cm, and the electrode diameter of 0.635 cm, the minimum distance between electrodes through the helium is 0.867 cm. The proposed operating pressure of the helium environment is 1520 Torr, resulting in 1317.84 Torr·cm. This value of Torr·cm exceeds the values of this chart, but it being greater than 1000 Torr·cm is key to this application. 1000 Torr·cm results in a breakdown voltage of greater than 10 kV, which is the maximum output of the hipot. Therefore, given the sample size and operating pressure of this system, it is unlikely to breakdown through the helium environment before the sample fails.

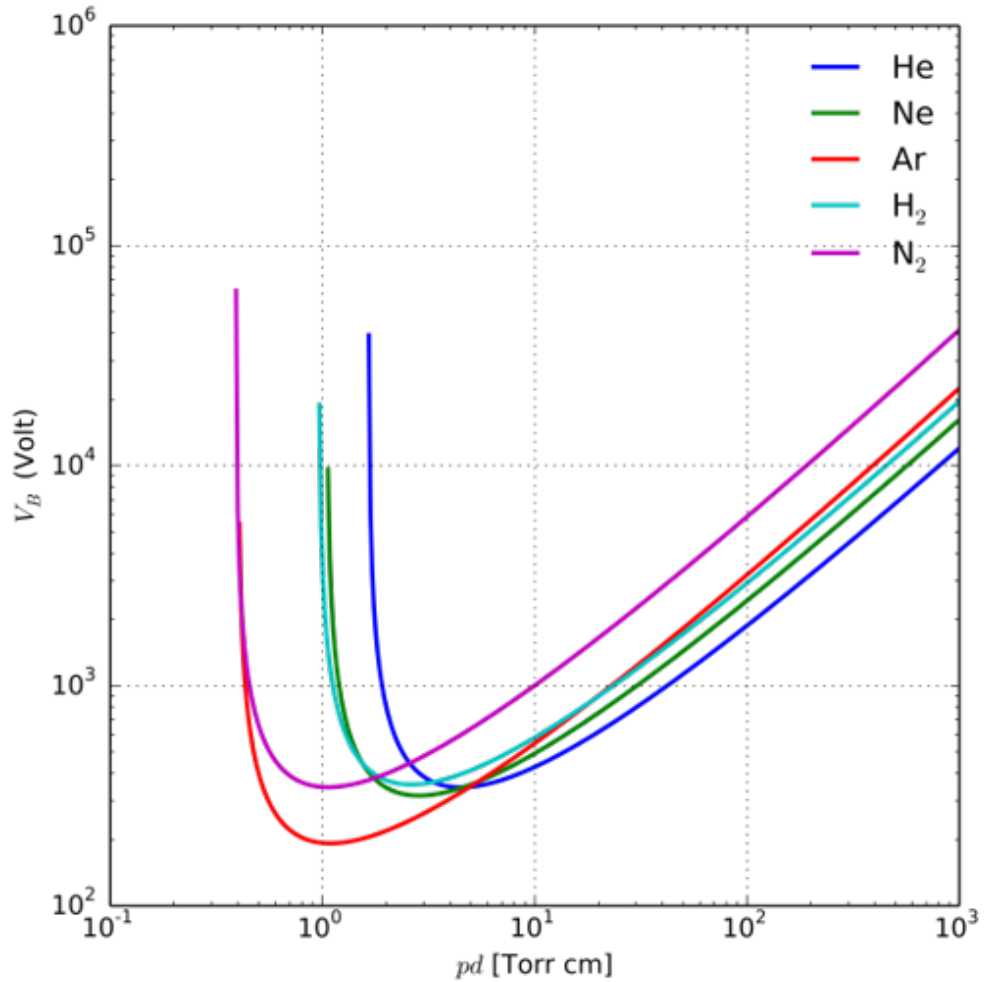


Figure 32. Paschen's curve, which plots combined values of pressure and distance against breakdown voltage [63].

5.2. Inner Chamber Design

The helium chamber designed for the purpose of testing dielectric and CTE properties of the PI/SiO₂ composite is comprised of two chambers, the outer vacuum chamber and the inner testing chamber. The design has gone through several iterations, and the one discussed here is the most recent. The entire chamber is made with ¼" (6.35 mm) 304 stainless steel, to keep thermal contraction consistent across the system. A flow

chart of the helium chamber can be seen in Figure 33. In order to reduce the effects of conduction, the penetrations to the inner chamber were minimized. One necessary penetration is the vacuum outlet which connects the testing chamber to the vacuum pump outside the chamber. This vacuum outlet will be used prior to testing, in order to empty the testing chamber before it is filled with helium. Once the testing chamber is vacuumed, the vacuum pump will be connected to the second vacuum outlet, which leads to the vacuum chamber. The pump will pull vacuum on this chamber throughout the duration of the test, and as long as the testing chamber is cooled. The helium inlet and outlet bayonet fittings attach to the cryogenic transfer hoses on the outside, and terminate inside the testing chamber. The lengths of the helium lines are different to prevent helium from flowing directly from the inlet to the outlet, and promote circulation throughout the testing chamber. Finally, the electrical feedthrough, which provides a means to power testing equipment and various sensors, is embedded within the wall of the testing chamber. The type K thermocouples used previously in this research become inaccurate below 92 K, so type T thermocouples will be strategically placed inside the inner chamber to get an accurate temperature measurement.

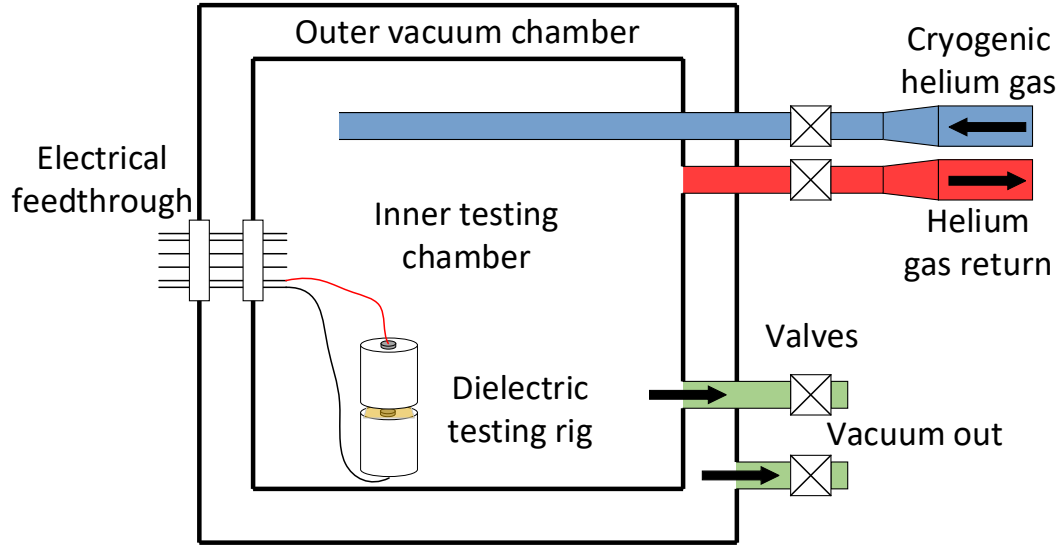


Figure 33. Flow chart of the helium chamber with a valve diagram.

The weight of the inner chamber is mostly supported by the three pipes connecting it to the wall of the outer chamber, which are the helium inlet, helium outlet, and the vacuum outlet. Although these three pipes are capable of supporting the inner chamber, rods made of thermally insulating G10 have been added as secondary supports. Further, reinforcement bands have been added on all but one wall of the testing chamber, in an effort to minimize deflection caused by the pressure differential. The front-facing side of the testing chamber, which does not feature a reinforcement band, instead has a CF flange with a metal gasket. This flange allows for access between the outer and inner chambers when the cover is removed. Samples can be loaded and removed from the testing chamber through this flange. It is important to note that while this flange will lead to the outside environment, when it is sealed there will be no contact with the outer chamber at this point, meaning there are no conductive heat losses. A SolidWorks rendering of the inner chamber can be seen in Figure 34. The dimensions of the inner

chamber are 7.5 in \times 7.5 in \times 8.5 in (19.05 cm \times 19.05 cm \times 21.59 cm), with the top and bottom plates being the longest. One wall has been cut away to view the inside of the chamber. The green device inside the inner chamber is the extensometer which will be used in the future to measure thermal contraction. Finally, multi-layer insulation (MLI) will coat the inner chamber in order to reduce any heat loss due to radiation, however this is not shown in the rendering [64]. MLI consists of alternating layers of thin plastic coated with a thin layer of metal, and netting spacer material.

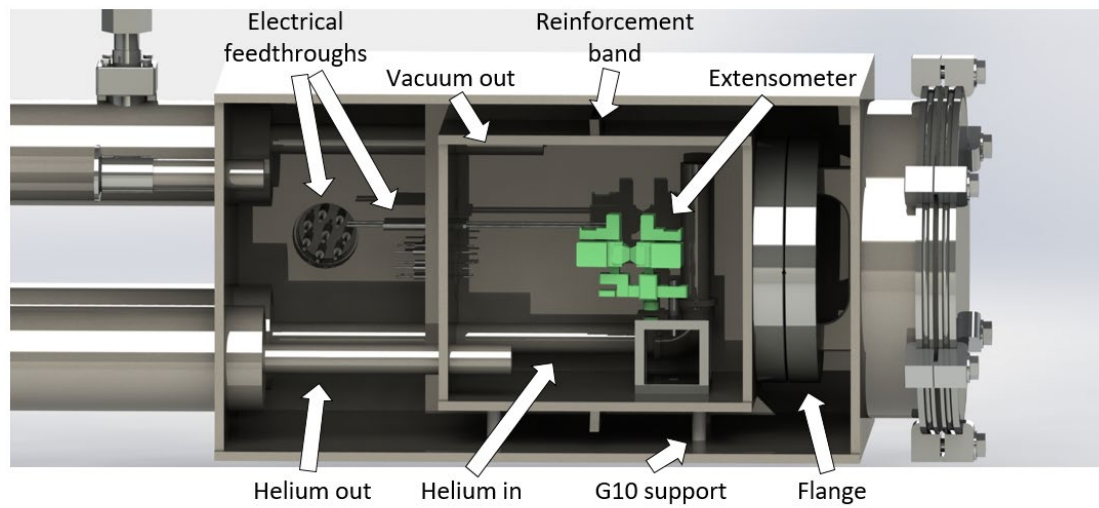


Figure 34. SolidWorks rendering of the inner testing chamber, contained within the outer vacuum chamber.

5.3. Outer Chamber Design

The outer chamber is designed to contain the inner testing chamber with as few connections as possible, while holding a strong vacuum to minimize heat losses. A rendering of the helium chamber can be seen in Figure 35. The chamber, not including

the pipes, is 10 in × 10 in × 17.5 in (25.4 cm × 25.4 cm × 44.45 cm) in length, with the top and bottom plates being the longest. On the front face of the outer chamber is a large flange which lines up with the flange on the inner chamber. Opening both of these flanges allows for access to the inner chamber from the outside to load and unload samples as well as access the electrical feedthrough. Another flange was placed on the side of the chamber to allow access to the piping, supports, and electrical feedthroughs which would be in the vacuum environment.

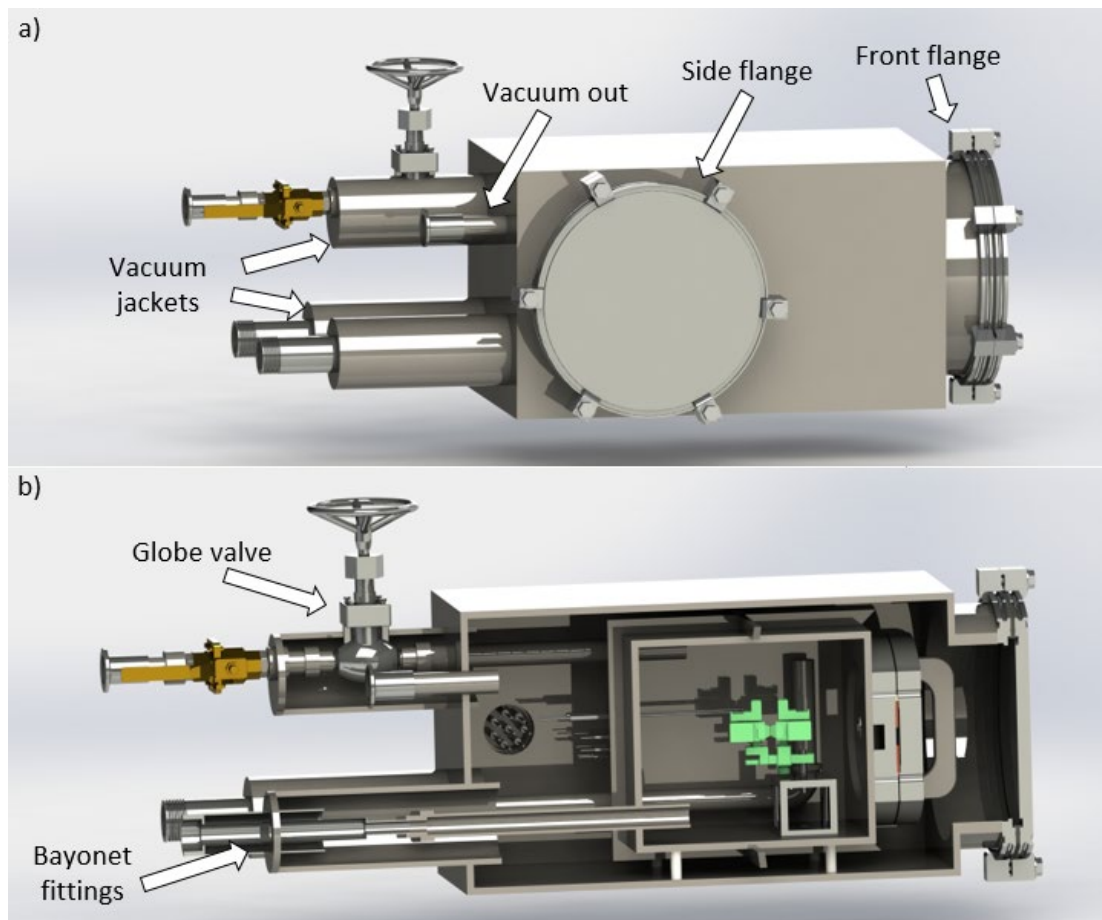


Figure 35. SolidWorks rendering of (a) the helium chamber, and (b) the cross-section of both chambers.

There are four pipes connecting to the rear of the outer chamber, which are two bayonet fittings contained in vacuum jackets, a KF fitting which attaches to the vacuum pump, and a cryogenic globe valve in a vacuum jacket. The globe valve will be used to control the flow when the inner chamber is being vacuumed, prior to tests. All vacuum jackets are connected to the vacuum contained in the outer chamber, meaning that they will be under an actively pulled vacuum for the duration of all tests. The pipes used for transfer of gaseous helium and connecting vacuum lines are all Schedule 40 stainless steel, with a ½” (12.7 mm) diameter.

5.4. Chamber Simulations

There are two main concerns regarding failure in the helium chamber, the operating pressure in the testing chamber, and the deflection of the pipes supporting the testing chamber. In order to address these concerns, simulations were run on SolidWorks to determine the amount of deflection and stress created by each of these factors. A simulation of the effects of operating pressure on the inner chamber walls can be seen in Figure 36. Given an operating pressure of 1520 Torr, and the dimensions of the 21.59 cm × 19.05 cm × 0.635 cm plates, the maximum deflection and stress can be modeled on a color scale. The maximum deflection was found to be 0.086 mm, while the maximum stress was 46.68 MPa. Assuming the yield strength of the stainless steel plates is 206.84 MPa, the resulting factor of safety is 4.43 [65]. Simulations were verified by a calculation program through MITCalc, which calculated a maximum deflection of 0.085 mm, and a maximum stress of 65.33 MPa [66]. These simulations were run prior to the addition of the reinforcement bands, which should reduce the deflection of the plates.

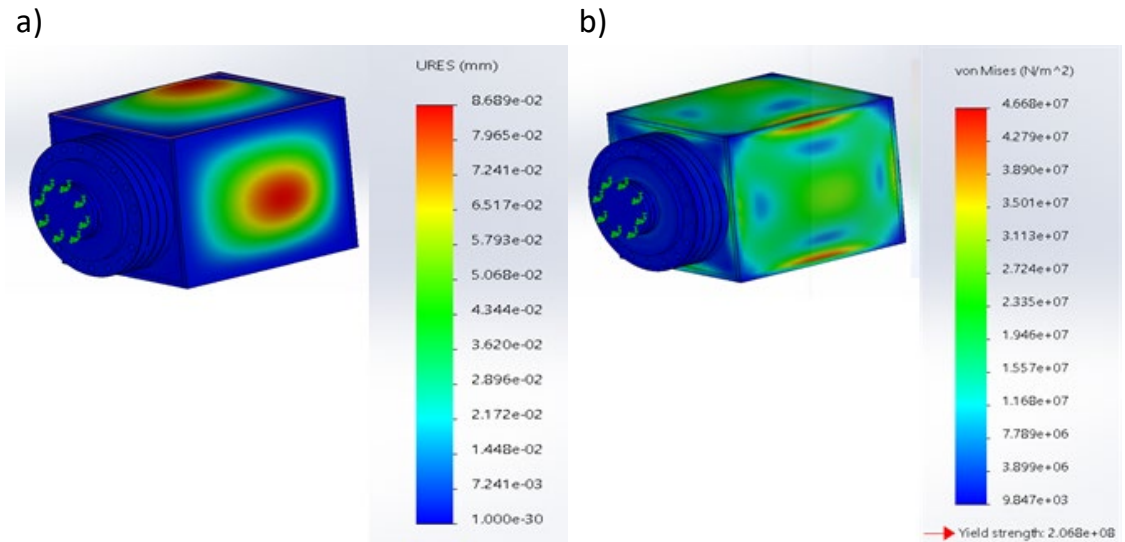


Figure 36. SolidWorks simulation of the effects of 1520 Torr operating pressure on the (a) deflection of the inner chamber, and (b) stress of the inner chamber.

The deflection of the pipes that support the weight of the inner chamber was also simulated to determine the maximum deflection and stress. Although the G10 supports will minimize the chamber's downward deflection, this simulation was run assuming those supports failed. Further, this simulation is of a single pipe, where in reality there will be three pipes taking the weight of the inner chamber. The results of this simulation can be seen in Figure 37. The Schedule 40 pipes have a ½" (12.7 mm) diameter, and the force of the inner chamber due to gravity was calculated to be 154.45 N. The simulated maximum deflection is 0.00891 mm, while the maximum stress is 83.47 MPa. Given a yield strength of 200.33 MPa, the resulting factor of safety is 2.4. Simulation results were verified via Roark's equation of stress for a beam which is fixed on one end and has a load at the other. Through this method, maximum deflection was found to be 0.00768 mm [67].

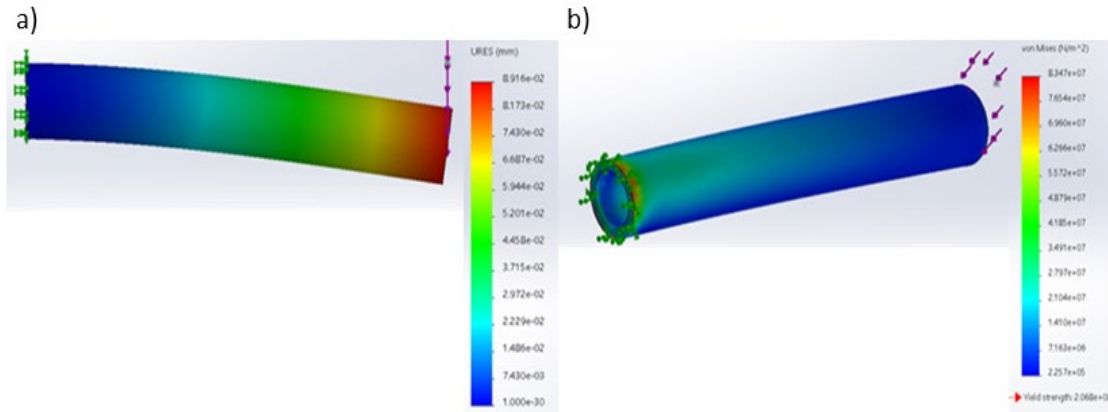


Figure 37. SolidWorks simulation of the effects of 154.45 N weight on (a) the deflection of a single pipe, and (b) the stress of a single pipe.

The design described herein is the latest of several iterations, and is the final as the manufacturing phase begins. However, it is expected that the design may undergo minor changes as it is manufactured if issues become apparent. As the chamber is to be built in-house, many pieces will be cut from larger bulk material. Many features are welded together, such as the chamber walls and vacuum jackets. Upon its completion, the project can move into the next and final phase: material testing in a helium-cooled cryogenic environment.

Chapter 6

Conclusions and Future Works

6.1. Summary

In this thesis, a potential dielectric for use on helium-cooled high-temperature superconducting cables is explored. Silicon dioxide is used as a nanoparticle filler inside of a polyimide host matrix. Given the right concentration of SiO₂, the composite will potentially have sufficient dielectric strength while matching the thermal contraction rate of the HTS cable. Composites were generated through both an ex situ and an in situ process, until in situ samples were found to have better dispersion and less particle agglomeration. The composites are prepared in the form of thin films, averaging 20 μm in thickness, for the characterization of their properties.

Composite samples were tested and examined through two main methods: dielectric breakdown testing and scanning electron microscopy. Dielectric breakdown tests occurred at both 300 K and 92 K. Tests performed at 92 K took place within a dewar containing liquid nitrogen, but the samples were not submerged in the LN₂. The samples showed a clear increase in dielectric strength when tested at cryogenic temperatures, which is attributed to the contraction of the polymer resulting in an increased density. Samples tested at room temperature averaged a dielectric strength of 175 kV/mm, while samples broken down in a cryogenic environment had an average dielectric strength of 275 kV/mm. Images taken on the SEM revealed uniform dispersion of the particles, as well as the particle size distribution. The majority of the nanoparticles were found to be less than 200 nm in diameter. Further, samples broken down at 92 K showed evidence of

treeing, a breakdown mechanism which involves the partial breakdown of a sample before failure occurs.

A helium-cooled cryogenic chamber was designed to house the testing equipment for dielectric breakdown and thermal contraction testing of the composites. This chamber should achieve temperatures lower than that of liquid nitrogen, and allow for tests similar to the composite's environment on the HTS cables. The helium chamber consists of the inner chamber, which is filled with helium and contained within the second chamber, the vacuum chamber. The vacuum surrounding the inner chamber will mitigate any convective heat loss, while limited connections work to reduce heat loss caused by conduction. Finally, multi-layer insulation will be used to reduce any heat loss due to radiation. This design is the latest of many iterations, and it will continue to be improved as the fabrication process begins.

The research performed herein provides insight to the fields of research involving nanocomposites, dielectric breakdown, and HTS cables aboard Navy ships. Throughout this research, works have been published describing the in situ fabrication process, providing a detailed set of instructions for the generation of PI/SiO₂ composites. Further, the behavior of the composites has also been discussed in these published works, specifically the performance in a cryogenic environment [68]. A dielectric strength comparison table can be seen in Table 3. The evidence of electrical treeing shown in Chapter 4 is fairly unique, as published works on this subject are limited. Finally, the work reported here has advanced Naval research involving HTS cables in a gaseous helium-cooled cryogenic environment. While not resolved, this issue is now better understood, and a solution seems more possible than ever before.

Table 3

Comparison of dielectric strength between this and other studies

Ref.	Host Matrix	Nanofiller	Testing Temperature (K)	Concentration (%)	Dielectric Strength (kV/mm)
[69]	Epoxy	Al ₂ O ₃ /SiC	300	0	23
				5	36
[32]	Polyimide	Nano-TiC	300	0	-
				5	34
[43]	Polyimide	Al ₂ O ₃	300	0	24
				5	21
[33]	Polyimide	BaTiO ₃	300	0	325
				5	311
[70]	Polystyrene	SiO ₂	300	0	400
				5	420
	Poly-4-Vinylpyridene	SiO ₂	300	0	490
				5	490
	Polymethyl Methacrylate	SiO ₂	300	0	815
				5	580
Polyimide	SiO ₂	300	0	570	
			5	530	
This Study	Polyimide	SiO ₂	300	0	268
				5	130
	Polyimide	SiO ₂	92	0	240
				5	277

6.2. Future Works

There are several facets of this research that have yet to be completed, and more that could be improved upon in the future. These facets have been retained and will be transferred to future researchers in order to facilitate the future works described herein. Refining these aspects and completing the unfinished tasks are essential to reaching the

end goal of this research, to coat an HTS cable with a PI/SiO₂ composite for use in a helium-cooled cryogenic environment.

- 1) Polyimide was chosen due to its strong dielectric strength and ease of use in a laboratory setting. However, the high imidization temperature of PI is not safe for HTS cable production. Given more time, another polymer should be explored as the host matrix. A comparative study could be conducted to determine if a different host polymer is more suitable for this application.
- 2) There are many factors to the in situ fabrication process. In the future, these factors can be adjusted in a parametric study in an effort to create more consistent silica particles. Greater consistency of particle diameter could potentially affect the properties of the composite material, as the particles above 100 nm in diameter may not have the same properties as those that are true nanoscale particles with diameter < 100 nm. Some factors that could be altered include but are not limited to: the time spent mixing the precursors separately, the time spent mixing the sol gel within PAA, and the ambient temperature during the mixing process.
- 3) All composite samples that underwent dielectric breakdown did so in a timely manner, relative to their fabrication. Ideally, a shelf life study could be conducted, in which samples created in one batch would be tested over time. A study such as this could determine if the properties of the composite change over time when not in use. The results found in this study would reveal whether or not the composite would need to be replaced on HTS cables, and how often.

- 4) Electron microscopy can be used to further examine the points of dielectric breakdown in the samples. Specifically, the particles contained within the area damaged by breakdown should be examined for any changes, such as sintering. Imaging the changes that these particles may undergo could lead to a greater understanding of the breakdown process and its lasting effects on a material.
- 5) The design of the helium chamber has been completed, and the next step in its completion is the manufacturing phase. During this phase, it is expected that minor issues will arise. For this reason, the manufacturing phase must be flexible, as improvements will need to be made to account for these flaws. Any improvement made to the chamber makes reaching the goal of 40 K more feasible.
- 6) The successful manufacture of the testing chamber will allow for testing of the effects of thermal cycling on the composite. Following a number of cooling cycles, the composite's dielectric strength and thermal contraction rate could be tested to determine if thermal cycling has an effect on these properties. The number of cooling cycles that take place prior to testing could be varied to produce more thorough results.
- 7) The composites are currently made in the form of thin films, which will need to change in order to be applied as the final product. One of the next major phases of this research is to develop a method to coat and cure the composite on a wire. Polymer extrusion is a common method used in the industry to coat wires, which involves pulling the wire through a vat filled with the polymer

which is used to coat the wire. Once coated, the wire moves through an oven to heat and cure the polymer in place. This method would be scalable, so that it could first be tested in a laboratory setting, then used on the full scale HTS cables, which may be as long as 100 feet.

- 8) Successfully coating a wire opens up two new testing methods. First, a coated wire could be placed in the chamber to be cooled and heated back to room temperature. Doing so would allow for the inspection of any failures in the composite caused by thermal cycling. Further, dielectric testing can be conducted on a coated wire. Testing could be performed using the point-plane method, in which a pointed electrode is pressed to the surface of the polymer on a wire, and the wire is grounded. A decrease in dielectric strength is expected when coating a wire in a dielectric, but the exact amount of the decrease is a key factor which should be determined. Achieving this, along with the other future works, moves this research closer to completion, and increases feasibility of implementation on HTS cables aboard Navy ships.

References

- [1] SuperPower Inc. "HTS TRANSMISSION CABLE." <http://www.superpower-inc.com/>.
- [2] R. Cava *et al.*, "Superconductivity in the quaternary intermetallic compounds LnNi₂B₂C," *Nature*, vol. 367, pp. 252-253, 01/20 1994.
- [3] Robert A. Hawsey and Satoshi Morozumi, "The Energy and Environmental Benefits of Superconducting Power Products," *Mitigation and Adaptation Strategies for Global Change*, vol. 10, no. 2, pp. 279-306, 2005/04/01 2005.
- [4] J. P. Stovall *et al.*, "Installation and operation of the Southwire 30-meter high-temperature superconducting power cable," *IEEE Transactions on Applied Superconductivity*, vol. 11, no. 1, pp. 2467-2472, 2001.
- [5] D. Lindsay, M. Roden, Dag Willen, Albert Keri, and B. Mehraban, "Operating experience of 13.2 kV superconducting cable system at AEP bixby station," vol. CIGRÉ, pp. B1-107, 08/20 2008.
- [6] Office of Naval Research, "Office of Naval Research Demonstrates Revolutionary New Counter-Mine Technology for Ships," ed, 2009.
- [7] R. A. Marshall, "The distributed energy store railgun, its efficiency, and its energy store implications," *IEEE Transactions on Magnetics*, vol. 33, no. 1, pp. 582-588, 1997.
- [8] Ronggang Cao and Guangwei Zhang, "Analysis of current characteristics of the electromagnetic rail gun based on HHT," *IEEJ Transactions on Electrical and Electronic Engineering*, vol. 13, no. 2, pp. 339-340, 2018.
- [9] John J. Holmes, *Reduction of a ship's magnetic field signatures* (Synthesis lectures on computational electromagnetics, #23). San Rafael, Calif. (1537 Fourth Street, San Rafael, CA 94901 USA): Morgan & Claypool Publishers, 2008.
- [10] Thomas H. Fikse Brian K. Fitzpatrick, William A. Lynch, "High temperature superconducting degaussing system," United States Patent Appl. 11/788,331, 2008.

- [11] F. Le Dorze, J. P. Bongiraud, J. L. Coulomb, P. Labie, and X. Brunotte, "Modeling of degaussing coils effects in ships by the method of reduced scalar potential jump," *IEEE Transactions on Magnetics*, vol. 34, no. 5, pp. 2477-2480, 1998.
- [12] J. T. Kephart, B. K. Fitzpatrick, P. Ferrara, M. Pyryt, J. Pienkos, and E. M. Golda, "High Temperature Superconducting Degaussing From Feasibility Study to Fleet Adoption," *IEEE Transactions on Applied Superconductivity*, vol. 21, no. 3, pp. 2229-2232, 2011.
- [13] National Museum of the Royal New Zealand Navy. "Degaussing Ships." <http://navymuseum.co.nz/>.
- [14] B. K. Fitzpatrick, J. T. Kephartl, and E. M. Golda, "Characterization of Gaseous Helium Flow Cryogen in a Flexible Cryostat for Naval Applications of High Temperature Superconductors," *IEEE Transactions on Applied Superconductivity*, vol. 17, no. 2, pp. 1752-1755, 2007.
- [15] (2007). *A National Effort to Introduce New Technology into the Power Delivery Infrastructure*.
- [16] H. Yumura *et al.*, "Phase II of the Albany HTS Cable Project," *IEEE Transactions on Applied Superconductivity*, vol. 19, no. 3, pp. 1698-1701, 2009.
- [17] H. Yumura *et al.*, "In-grid demonstration of long-length "3-in-One" HTS cable (Albany Project)," *SEI Technical Review*, pp. 69-79, 04/01 2009.
- [18] M. Santosh, "The Promising Role of Superconductivity in Cable Power Applications," *Journal of Electrical Engineering*, vol. 6, pp. 295-298, 2018.
- [19] C. Gu, Y. Zhang, F. Li, and W. Yuan, "Economic analysis of interconnecting distribution substations via superconducting cables," in *2012 IEEE Power and Energy Society General Meeting*, 22-26 July 2012 2012, pp. 1-5.
- [20] W. Yuan, S. Venuturumilli, Z. Zhang, Y. Mavrocostanti, and M. Zhang, "Economic Feasibility Study of Using High-Temperature Superconducting Cables in U.K.'s Electrical Distribution Networks," *IEEE Transactions on Applied Superconductivity*, vol. 28, no. 4, pp. 1-5, 2018.

- [21] M. Kosaki, "Research and development of electrical insulation of superconducting cables by extruded polymers," *IEEE Electrical Insulation Magazine*, vol. 12, no. 5, pp. 17-24, 1996.
- [22] M. Kosaki, M. Nagao, Y. Mizuno, N. Shimizu, and K. Horii, "Development of extruded polymer insulated superconducting cable," *Cryogenics*, vol. 32, no. 10, pp. 885-894, 1992/01/01/ 1992.
- [23] J. F. Heacock and C. E. Berr, "Polyimides—new high temperature polymers: H-film, a polypyromellitimide film," *Polymer Engineering & Science*, vol. 5, no. 2, pp. 105-110, 1965.
- [24] Jack Ekin and George Zimmerman, "Experimental Techniques for Low-Temperature Measurements: Cryostat Design, Material Properties, and Superconductor Critical-Current Testing," *Physics Today - PHYS TODAY*, vol. 60, 05/01 2007.
- [25] Uday Burman and Praveen Kumar, "Chapter 5 - Plant Response to Engineered Nanoparticles," in *Nanomaterials in Plants, Algae, and Microorganisms*, D. K. Tripathi, P. Ahmad, S. Sharma, D. K. Chauhan, and N. K. Dubey Eds.: Academic Press, 2018, pp. 103-118.
- [26] Anna C. Balazs, Todd Emrick, and Thomas P. Russell, "Nanoparticle Polymer Composites: Where Two Small Worlds Meet," *Science*, vol. 314, no. 5802, pp. 1107-1110, 2006.
- [27] Masakatsu Kochi, Rikio Yokota, Taka Yuki Iizuka, and Itaru Mita, "Improving tensile mechanical properties of aromatic polyimides by thermal imidization after cold drawing of poly (amic acids)," *Journal of Polymer Science Part B: Polymer Physics*, vol. 28, no. 13, pp. 2463-2472, 1990.
- [28] Sigma-Aldrich. Poly(pyromellitic dianhydride-co-4,4'-oxydianiline), amic acid solution [Online] Available: <https://www.sigmaaldrich.com/united-states.html>
- [29] X. Cui *et al.*, "Mechanical and dielectric properties of polyimide/silica nanocomposite films," *Plastics, Rubber & Composites*, Article vol. 44, no. 10, pp. 435-439, 2015.

- [30] Young-Jae Kim, Jong-Heon Kim, Shin-Woo Ha, Dongil Kwon, and Jin-Kyu Lee, "Polyimide nanocomposites with functionalized SiO₂ nanoparticles: enhanced processability, thermal and mechanical properties," *RSC Advances*, 10.1039/C4RA04952G vol. 4, no. 82, pp. 43371-43377, 2014.
- [31] Der-Jang Liaw, Kung-Li Wang, Ying-Chi Huang, Kueir-Rarn Lee, Juin-Yih Lai, and Chang-Sik Ha, "Advanced polyimide materials: Syntheses, physical properties and applications," *Progress in Polymer Science*, vol. 37, no. 7, pp. 907-974, 2012/07/01/ 2012.
- [32] Qian-shan Xia, Ling Weng, Li-wen Yan, Li-zhu Liu, Mao-chang Cao, and Jun-wang Liu, "Preparation and dielectric properties of nano-TiC/polyimide composite films as embedded-capacitor application," in *Ifostr*, 28 June-1 July 2013 2013, vol. 1, pp. 230-232.
- [33] Shuangshuang Yue, Baoquan Wan, Yunying Liu, and Qiwei Zhang, "Significantly enhanced dielectric constant and energy storage properties in polyimide/reduced BaTiO₃ composite films with excellent thermal stability," *RSC Advances*, 10.1039/C8RA10434D vol. 9, no. 14, pp. 7706-7717, 2019.
- [34] Y. Z. Hu, D. J. Diehl, Q. Liu, C. Y. Zhao, and E. A. Irene, "In situ real time measurement of the incubation time for silicon nucleation on silicon dioxide in a rapid thermal process," *Applied Physics Letters*, vol. 66, no. 6, pp. 700-702, 1995.
- [35] K. Achuthan, J. Curry, M. Lacy, D. Campbell, and S. V. Babu, "Investigation of pad deformation and conditioning during the CMP of silicon dioxide films," *Journal of Electronic Materials*, vol. 25, no. 10, pp. 1628-1632, 1996/10/01 1996.
- [36] C. J. Huang, S. Y. Fu, Y. H. Zhang, B. Lauke, L. F. Li, and L. Ye, "Cryogenic properties of SiO₂/epoxy nanocomposites," *Cryogenics*, vol. 45, no. 6, pp. 450-454, 2005/06/01/ 2005.
- [37] K. P. Chow and G. A. Millos, "Measurements of modulus of elasticity and thermal contraction of epoxy impregnated niobium-tin and niobium-titanium composites," *IEEE Transactions on Applied Superconductivity*, vol. 9, no. 2, pp. 213-215, 1999.
- [38] Paul R Gray, Paul Hurst, Robert G Meyer, and Stephen Lewis, *Analysis and design of analog integrated circuits*. Wiley, 2001.

- [39] Pavel V. Komarov, Yu-Tsung Chiu, Shih-Ming Chen, and Peter Reineker, "Investigation of Thermal Expansion of Polyimide/SiO₂ Nanocomposites by Molecular Dynamics Simulations," *Macromolecular Theory and Simulations*, vol. 19, no. 1, pp. 64-73, 2010.
- [40] Chul Han Kim, Sung-Kyu Kim, Lukas Graber, and Sastry V. Pamidi, "Cryogenic Thermal Studies on Terminations for Helium Gas Cooled Superconducting Cables," *Physics Procedia*, vol. 67, pp. 201-207, 2015/01/01/ 2015.
- [41] N. Suttell, C. H. Kim, J. Ordonez, D. Shah, L. Graber, and S. Pamidi, "Thermal Modeling of Gaseous Helium as a Cryogen for High Temperature Superconducting Cable Components," *IEEE Transactions on Applied Superconductivity*, vol. 25, no. 3, pp. 1-5, 2015.
- [42] Hsin-Wei Lin and Chung-Sung Tan, "Preparation of polyamic acid and polyimide nanoparticles by compressed fluid antisolvent and thermal imidization," *The Journal of Supercritical Fluids*, vol. 99, pp. 103-111, 2015/04/01/ 2015.
- [43] Hongyan Li, Gang Liu, Bin Liu, Wei Chen, and Shoutian Chen, "Dielectric properties of polyimide/Al₂O₃ hybrids synthesized by in-situ polymerization," *Materials Letters*, vol. 61, no. 7, pp. 1507-1511, 2007/03/01/ 2007.
- [44] Werner Stöber, Arthur Fink, and Ernst Bohn, "Controlled growth of monodisperse silica spheres in the micron size range," *Journal of Colloid and Interface Science*, vol. 26, no. 1, pp. 62-69, 1968/01/01/ 1968.
- [45] Xiao-Dong Wang *et al.*, "Preparation of spherical silica particles by Stöber process with high concentration of tetra-ethyl-orthosilicate," *Journal of Colloid and Interface Science*, vol. 341, no. 1, pp. 23-29, 2010/01/01/ 2010.
- [46] Lok P. Singh *et al.*, "Sol-Gel processing of silica nanoparticles and their applications," *Advances in Colloid and Interface Science*, no. 214, pp. 17-37, 2014.
- [47] Michael McCaffrey, Harrison Hones, Jordan Cook, Robert Krchnavek, and Wei Xue, "Geometric analysis of dielectric failures in polyimide/silicon dioxide nanocomposites," *Polymer Engineering & Science*, vol. 59, no. 9, pp. 1897-1904, 2019.

- [48] Wenjuan Chen, Wei Chen, Baoqing Zhang, Shiyong Yang, and Chen-Yang Liu, "Thermal imidization process of polyimide film: Interplay between solvent evaporation and imidization," *Polymer*, vol. 109, pp. 205-215, 2017/01/27/ 2017.
- [49] J. McPherson, J-Y. Kim, A. Shanware, and H. Mogul, "Thermochemical description of dielectric breakdown in high dielectric constant materials," *Applied Physics Letters*, vol. 82, no. 13, pp. 2121-2123, 2003.
- [50] N. Klein, "Electrical Breakdown in Thin Dielectric Films," *Journal of The Electrochemical Society*, vol. 116, no. 7, p. 963, 1969.
- [51] P. P. Pronko *et al.*, "Avalanche ionization and dielectric breakdown in silicon with ultrafast laser pulses," *Physical Review B*, vol. 58, no. 5, pp. 2387-2390, 08/01/ 1998.
- [52] E. J. Lauer and C. J. Lauer, "Electron avalanche on a dielectric-vacuum interface," *IEEE Transactions on Dielectrics and Electrical Insulation*, vol. 24, no. 2, pp. 1295-1299, 2017.
- [53] A. Padovani, D. Z. Gao, A. L. Shluger, and L. Larcher, "A microscopic mechanism of dielectric breakdown in SiO₂ films: An insight from multi-scale modeling," *Journal of Applied Physics*, vol. 121, no. 15, p. 155101, 2017.
- [54] Y. Ehara, M. Naoe, K. Urano, H. Kishida, M. Matsuyama, and T. Ito, "Fractal analysis of the treeing process from luminous discharge image and measurement of discharge magnitude," *IEEE Transactions on Dielectrics and Electrical Insulation*, vol. 5, no. 5, pp. 728-733, 1998.
- [55] X. Chen, Y. Xu, X. Cao, S. J. Dodd, and L. A. Dissado, "Effect of tree channel conductivity on electrical tree shape and breakdown in XLPE cable insulation samples," *IEEE Transactions on Dielectrics and Electrical Insulation*, vol. 18, no. 3, pp. 847-860, 2011.
- [56] Ming-Yan Zhang, Shu-Jin Zeng, Yong Fan, Pei-Hong Zhang, and Qing-Quan Lei, "Dielectric and conduction properties of polyimide/silica nano-hybrid films," *Polymer Composites*, vol. 29, no. 6, pp. 617-622, 2008.

- [57] T. Tanaka, "Dielectric nanocomposites with insulating properties," *IEEE Transactions on Dielectrics and Electrical Insulation*, vol. 12, no. 5, pp. 914-928, 2005.
- [58] Hoikwan Lee, Nicholas J. Smith, Carlo G. Pantano, Eugene Furman, and Michael T. Lanagan, "Dielectric Breakdown of Thinned BaO–Al₂O₃–B₂O₃–SiO₂ Glass," *Journal of the American Ceramic Society*, vol. 93, no. 8, pp. 2346-2351, 2010.
- [59] K. Tienda *et al.*, "Investigation of glass transition temperature for polyimide composites: Study of influence of specimen thickness and thermo-mechanical response," ed, 2013, pp. 2554-2572.
- [60] C. Laurent and C. Mayoux, "Partial discharge. XI. Limitations to PD as a diagnostic for deterioration and remaining life," *IEEE Electrical Insulation Magazine*, vol. 8, no. 2, pp. 14-17, 1992.
- [61] ASME, "Boiler and Pressure Vessel Code," *An International Code*.
- [62] U.S. Particle Accelerator School, "Elements of Cryogenics System Design," *Cryogenic Safety*.
- [63] Robert Keatch, "Principles of plasma discharges and material processing: M.A. Lieberman and A.J. Lichtenberg, John Wiley, New York, 1994, 572 pp," *Microelectronics Journal*, vol. 27, no. 8, p. 804, 1996/11/01/ 1996.
- [64] S. L. Bapat, K. G. Narayankhedkar, and T. P. Lukose, "Performance prediction of multilayer insulation," *Cryogenics*, vol. 30, no. 8, pp. 700-710, 1990/08/01/ 1990.
- [65] American Metals Co. 304 Stainless Steel Technical Data Sheet [Online] Available: <https://www.metalslshims.com/>
- [66] *Plate Deflection and Stress*. (2009). www.mitcalc.com.
- [67] C. Young Warren, G. Budynas Richard, and M. Sadegh Ali, *Roark's Formulas for Stress and Strain, Eighth Edition*, 8th ed. / ed. New York: McGraw-Hill Education (in eng), 2012.

- [68] H. M. Hones *et al.*, "Polyimide-based Nanocomposites as Low-Temperature Dielectrics," in *2019 IEEE 14th Nanotechnology Materials and Devices Conference (NMDC)*, 27-30 Oct. 2019 2019, pp. 1-4.
- [69] M Hoseini, G Dini, and M Bahadori, "Dielectric strength and mechanical properties of epoxy resin filled with self-propagating high-temperature synthesized Al₂O₃/SiC nanoparticles," *Journal of Composite Materials*, vol. 0, no. 0, p. 0021998319891202.
- [70] Soliman Abdalla, Fahad Al-Marzouki, Abdullah Obaid, and Salah Gamal, "Effect of Addition of Colloidal Silica to Films of Polyimide, Polyvinylpyridine, Polystyrene, and Polymethylmethacrylate Nano-Composites," (in eng), *Materials (Basel)*, vol. 9, no. 2, p. 104, 2016.